Chapter 5

Modeling of the surface laser treatment of a thermal barrier coating

Abstract

A numerical model was developed to simulate the interaction of a CO_2 laser with a typical plasma-sprayed porous ceramic thermal barrier coating. The objective was to develop a tool, specifically designed for this application, by which the laser characteristics (beam diameter, intensity and energy distribution, etc.), time of interaction, material properties (total porosity and pore shape, absorption to a specific wavelength, etc), etc. could be varied and therefore allow to study their influence on the resulting thickness and width of the treated/melted region at the surface. Moreover, it was also developed a subsequent thermal strain/stress finite element model by which we could use the temperature distribution as an input and determine the consequent thermal stress distribution in the material. The first approach was based on a 3-D transient heat transfer finite difference analysis, and the second was based on a 2-D static stress finite element analysis.

1. Introduction

Theoretical models could offer cost-effective and highly flexible means for analyzing and optimizing laser surface processing. However, an accurate theoretical model for analyzing the thermal fields is thus extremely complicated and requires numerical approaches, e.g., finite difference method (FDM) or finite element method (FEM) [1].

Recently, several experimental studies have been performed to determine the effect of a surface laser treatment of a thermal barrier coating (TBC) [2-12]. However, although there are many theoretical studies concerning surface laser treatments, none is applied to thermal barrier coatings in particular. There are several theoretical works to study the effects of laser interaction with materials [1, 13-31]. Many different types of materials such as metal matrix composites

[26], clay tiles [27, 32], dental enamel [30], magnesia partially stabilized zirconia [17], etc. have been evaluated. Moreover, different types of lasers have also been modeled: CO_2 [17, 26, 29, 30], Er:YAG [30], high-power diode laser [27]. A recent review by Mackwood and Crafer [25] on thermal modelling of laser welding and related processes show on one hand the importance of the modelling approach, and on the other hand the complexity and variety of approaches to this problem. The analytic descriptions have a limited complexity, and typically use constant material properties. The numerical studies allow more processes to be included, the complexity being only limited by the amount of processor time available. One very often runs into a problem whose particular conditions have no analytical solution, or where the analytical solution is even more difficult to implement than a suitably accurate numerical solution [33].

The finite element method [34-37] has been so well established that today it is considered to be one of the best methods for solving a wide variety of practical problems efficiently. One of the main reasons for the popularity of the method in different fields of engineering is that once a general computer program is written, it can be used for the solution of any problem simply by changing the input data. The finite element method is a numerical method that can be used for the accurate solution of complex engineering problems. Several works applied the method to ceramic materials [1, 16, 27]. Nevertheless, they do not include mesoscopic features, of the order of a few microns, that actually define structures and thermal properties of materials like the plasma sprayed coatings. Vila Verde et al. [29, 30] studied the interaction of a laser beam with dental enamel, modelled using a finite element program, but including features with sizes as small as 0.1 μm. Her results show how important it may be to include mesostructures in the calculation, since the temperature and stress distributions strongly depend on these features.

A proper modelling of the laser-glazing process can provide some insight of how the laser affects the structure of the TBC, and gives some understanding of how to better control the process. But to make a proper modelling one has to account for several things, namely the morphology of the surface, the porosity of the sample, the melting and evaporation, the stresses generated. In this work is described a computational model which helps to better understand the influence of the process variables, such as laser characteristics and material properties, in the laser treatment of plasma-sprayed thermal barrier coatings.

2. Details of the Model

2.1. Construction of TBC workpiece

The first step taken was to build the sample workpiece in accordance with the system under study. For that purpose, since the finite difference method would be used to perform the thermal analysis, the workpiece was created from a 3D grid with elements with equal dimensions and evenly spaced. Furthermore, the elements were considered isotropic, i.e. the material properties are independent of direction. Nevertheless, these restrictions may be easily modified according the needs of the problem under study.

The flowchart illustrated in Fig 5.1 describes the procedures used to create the virtual TBC workpiece, in which the main steps are:

1. Creation of a 3D bulk brick (3D array) with the appropriate dimensions and number of elements.

2. Generation of disk-shaped porosity by:
   - randomizing the x,y and z coordinates of the centre of the horizontal disk
   - randomizing the radius of the disk (< max. radius)
   - subtracting the disk with thickness=1 element to the workpiece

3. Generation of surface roughness by:
   - creating a meshed flat plane
   - randomizing the height coordinate of each element, z, above or below the plane
   - smooth the surface by averaging the height of the 8 adjacent elements, for each element
   - subtract the generated surface to the workpiece

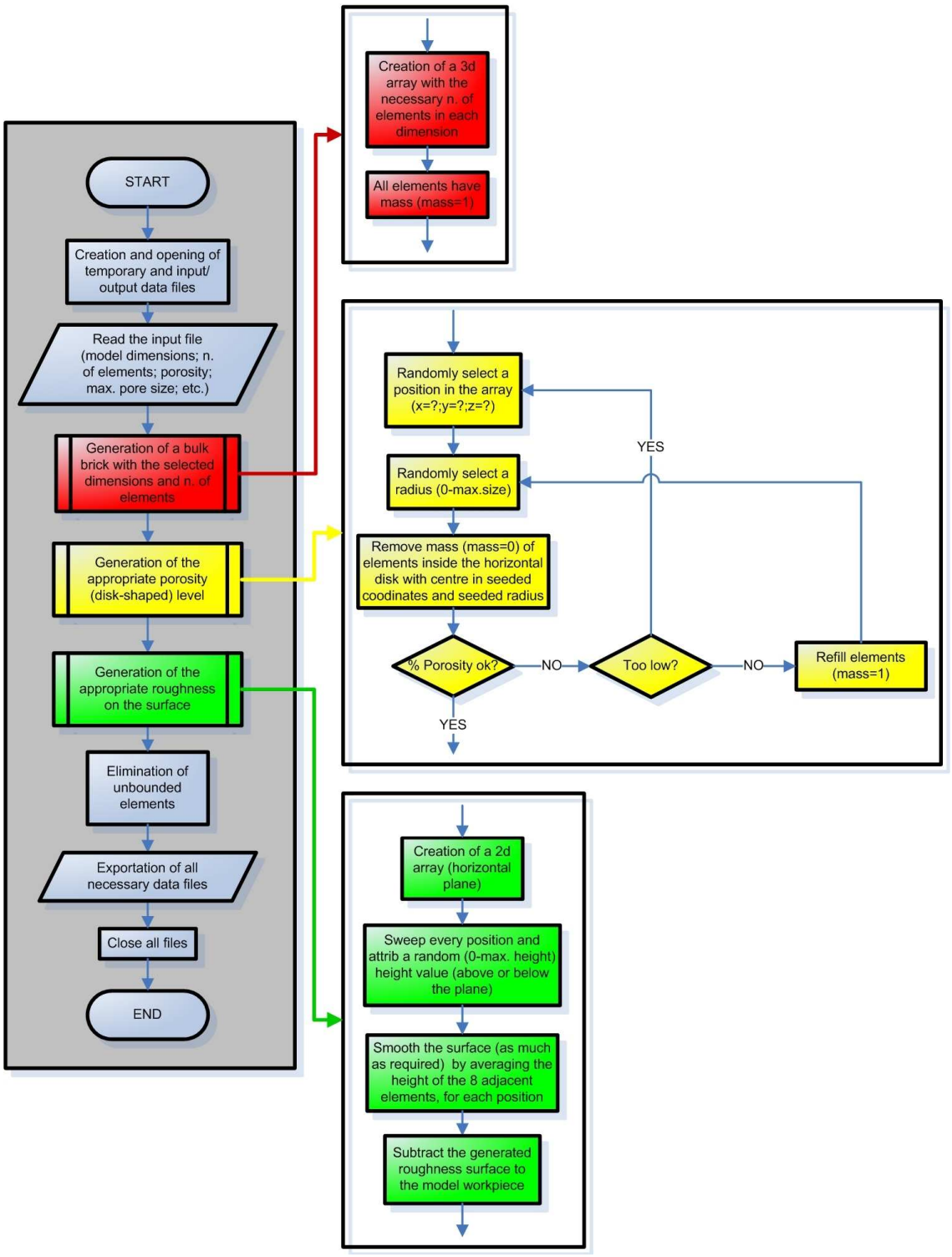

Fig 5.1. Flowchart diagram of the construction of the virtual 3D TBC workpiece.

A 3D sample was produced in emulation of the pictures we have from SEM micrographs (Fig 5.2) of coatings as they come from the plasma-spraying process.

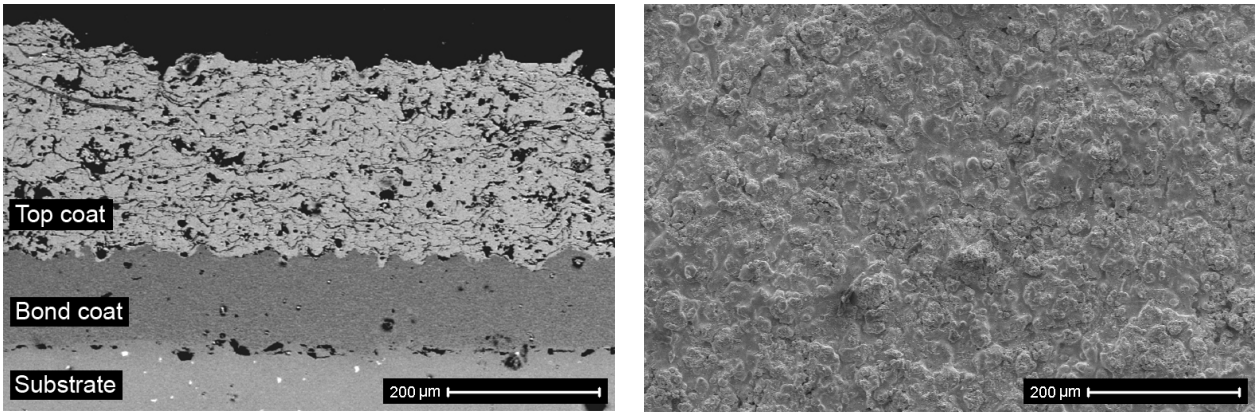

(a) (b)

Fig 5.2. Typical characteristics of a plasma-sprayed TBC; a) cross-section view showing the porous microstructure and b) top view of the surface showing the typical roughness.

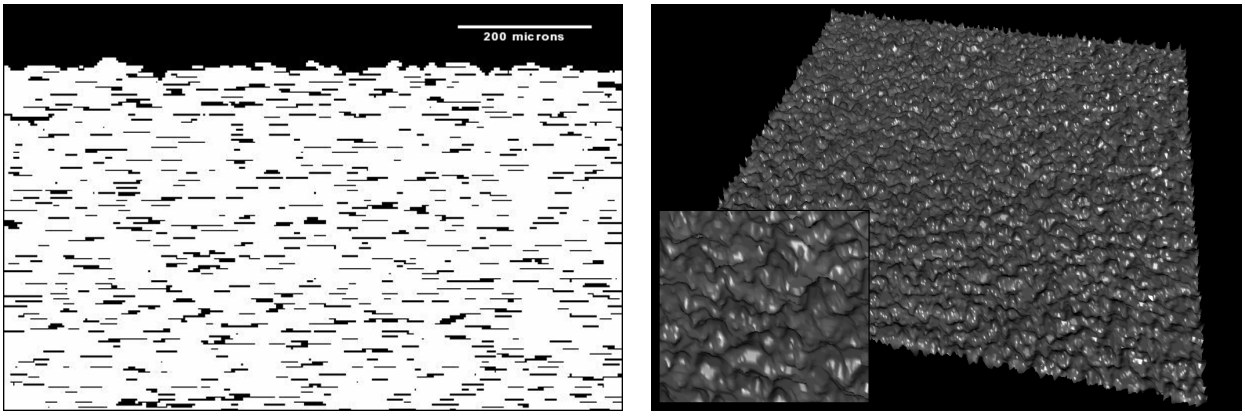

(a) b)

Fig 5.3. View of the modelled TBC: (a) cross-section view illustrating the microstructure; (b) top view of a 1.5x1.5mm^2 surface.

Fig 5.2 and Fig 5.3 show a comparison between experimental SEM micrographs and the computer generated workpiece. It can be seen that both the porosity and the surface morphology were taken into account. This is important since they affect the heat transfer and the absorption of the incident laser radiation. The modeled porosity consists of disk-shaped voids with random diameter in the range 3.75-15µm and 3.75µm thick. The porosity level is a parameter that can be adjusted and a so in this case 10% of the total volume was chosen, based on the values determined by Portinha and co-workers [38]. The morphology of the surface has been designed to achieve the same appearance and level of roughness of a real sample, Ra~10-20µm, as measured experimentally [3].

2.2. Materials properties

In order to obtain results as much accurate as possible, the material properties have to be carefully chosen. The material properties used in the model and presented herein are for YSZ or if not available, for pure ZrO_2 (tetragonal).

Table 5.1. Material properties of the zirconia workpiece used in the modeling.

Density (bulk ZrO_2) kg/m^3	6040 [39]
Initial temperature (°C)	25
Melting temperature (°C)	2690 [40]
Evaporation temperature (°C)	4300 [40]
Latent heat of fusion (J/kg)	708000 [40]
Latent heat of evaporation (J/kg)	5230000 [40]
Thermal expansion coefficient (°C^{-1})	10.3x10^{-6} [39]
Young's Modulus (GPa)	210 [39]
Poisson's ratio	0.23 [39]
Emissivity	0.5 [41]
Specific heat (J/(kg.°C)	according to eq. 5.1 [42]
Thermal conductivity (W/(m.°C)	according to eq. 5.2 [42]

The specific heat was considered dependent on the temperature and so changed from point to point in the sample and as the sample was being heated. The equation for the dependence on temperature was taken from [42] and used only below the melting point. Above it, the Cp was considered constant since no data available for the liquid phase was found.

$$c_p \ (J/(kg^\circ C)) = \begin{cases} 2.74 + 0.795T - 6.19\times10^{-4}T^2 + 1.71\times10^{-7}T^3 & \text{if } T_r \le T \le T_m \\ 990.67 & \text{if } T \ge T_m \end{cases} \quad (5.1)$$

Also, the thermal conductivity was made dependent on temperature and the equation which describes this behavior is given by [42]:

$$k \ (W/(m^\circ C)) = 1.71 + 0.21\times10^{-3}T + 0.116\times10^{-6}T^2 \quad (5.2)$$

To make easier the interpretation of eq. 5.1 and eq. 5.2, in Fig 5.4 are represented the mentioned properties as a function of temperature, in the range of interest.

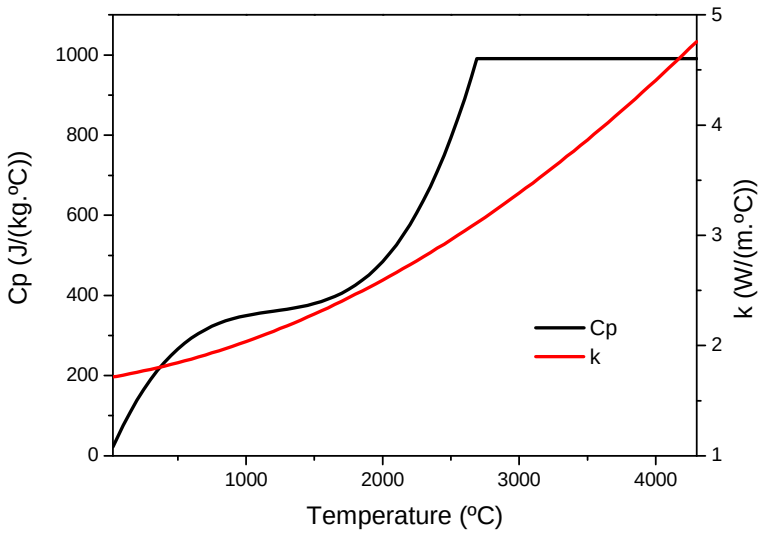

Fig 5.4. Dependence of the specific heat (cp) and thermal conductivity (k) on the temperature as described in eqs. 5.1 and 5.2 respectively.

2.3. The laser beam

The full spot of a CO_2 laser beam was simulated. The beam energy distribution was approximated to the real CO_2 laser used in the experiments. It consisted of a beam with a TEM_{01^*} (superposition of modes TEM_{01} and TEM_{10}) which is characterized by a mixture of a Gaussian and Doughnut modes given by:

$$I(x,y) = I_0\left[f + (1-f)\left(\frac{x^2+y^2}{r^2}\right)\right]\exp\left(-\frac{x^2+y^2}{r^2}\right) \qquad (5.3)$$

where f is the fraction of the Gaussian mode, r the beam radius and I_o the beam output energy given by:

$$I_0 = \frac{P}{\pi.r^2}\text{, where } P \text{ is the output laser power} \qquad (5.4)$$

The modeled beam energy intensity distribution along the radius based on eqs. 5.3 and 5.4. and in Table 5.2 is illustrated in Fig 5.5.

Table 5.2. Variable parameters used in the laser beam modeling.

F	r (m)	P(W)
0.35	0.215×10^{-3}	500

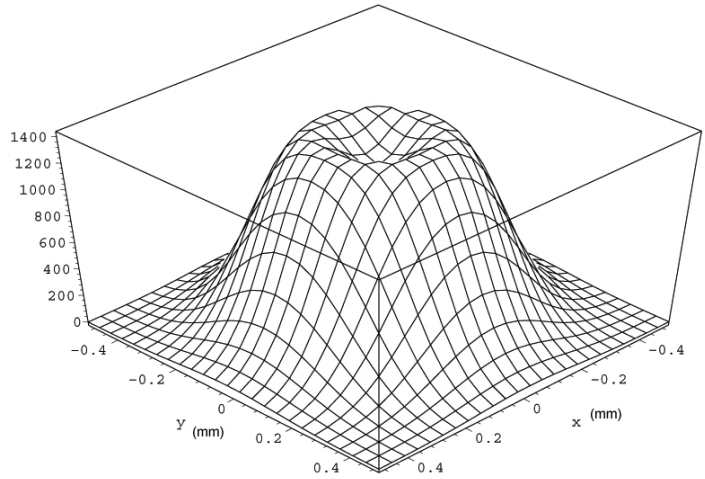

Fig 5.5. Energy intensity distribution along the radius of simulated laser beam.

The beam was also modeled as a volumetric heating source where the intensity at a given depth z of absorbing material is:

$I(z) = I_0 \exp(-\alpha z)$, being α the absorption coefficient (5.5)

Theoretically, most ceramic materials are poor absorbers of heat and much less reflective than metals to long infrared wavelengths. Therefore, CO_2 laser energy tends to penetrate more effectively such materials than metals [1]. Experimental studies [43, 44] have shown the enormous differences in the absorption lengths of CO_2 laser for ceramics and metals. Thus, the laser induced thermal fields should be more appropriately modeled with volumetric heating sources.

The laser beam and workpiece were assumed static with respect to the coordinate system and the laser intensity variation with time was taken as constant. The time of interaction of the laser beam with the ceramic coating has been set to 5 ms and was determined by:

$$\text{Pulse} = \frac{d}{v} \quad (5.6)$$

where d is the laser beam diameter and v is the laser scanning speed. For the simulation we have chosen a beam diameter of 0.43mm, and a scanning speed of 5000 mm/min, based on the experimental work described in chapter 3.

2.4. Description of the thermal model

A program based in the finite difference method was made to calculate the energy deposition by the incident laser beam, the corresponding increase in temperature, heat conduction to adjacent elements, eventual melting of the material and evaporation, as a function of time, in a 3D transient heat transfer approach. A flowchart diagram which describes the procedures of the program developed is illustrated in Fig 5.6.

The finite difference method [45, 46] begins with the discretization of space and time such that there is an integer number of points in space and an integer number of times at which we calculate the field variables, in this case the temperature. For simplicity an equal spacing of the points is assumed, in the three directions, with intervals of size $\Delta x = x_{i+1} - x_i$ (grid with points evenly spaced), and equal spacing of the timesteps t_n at intervals of $\Delta t = t_{n+1} - t_n$. This simplifies the system considerably, since it deals with a finite number of temperature values at a finite number of locations and times. Being the properties isotropic, the number of explicit timesteps (iterations) required is equal to the total time divided by the maximum simulated timestep size.

The numerical method used is called explicit timestepping, and uses the field values of only the previous timestep to calculate those of the next.

2.4.1. Laser energy deposition and absorption

The laser optical energy is transferred to the workpiece material and absorbed according to eq. 5.5 which describes an exponential decay with depth. The porosity was taken into account and considered as non-absorbing voids, allowing the energy to pass through and be absorbed by the elements beneath. The absorbed optical energy is fully converted into thermal energy.

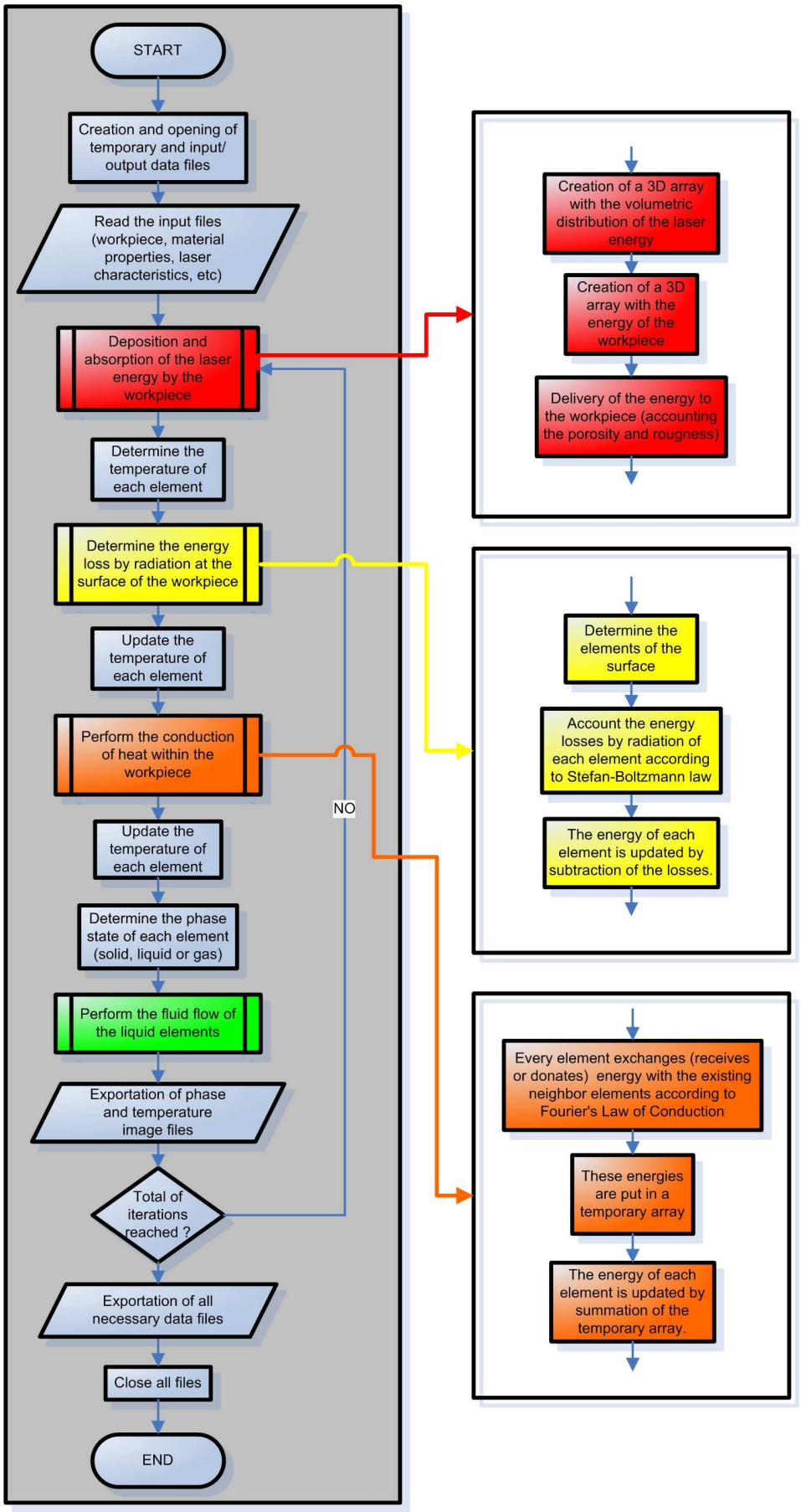

Fig 5.6. Flowchart diagram of the model approach used to perform the thermal analysis.

The absorption coefficient at the CO_2 laser wavelength (10.6 microns) for YSZ or ZrO_2 could not be found in literature and so it was measured in a real sample and estimated to be between 20000 m^{-1} and 50000 m^{-1}. This large interval was due to the roughness of the sample and the inhomogeneity in porosity, which limited the precision of the measurement. The influence of the surface roughness on the absorption of light, particularly in the thermal barrier coating field, has been demonstrated by Chwa and Ohmori [11].

2.4.2. Losses of energy by radiation at the surface

All elements at the top surface are considered to emit energy by radiation depending on their temperatures according to the Stefan–Boltzmann law:

$$P = e\sigma A(T^4 - T_r^4) \tag{5.7}$$

where P is the emitted power, e is the emissivity of the material, σ is the Stefan-Boltzmann constant, A is the emitting surface area, T is the temperature of the emitting material and T_r is the temperature of the surroundings (room temperature, 25°C).

2.4.3. Energy transfer by conduction

This routine is intended to allow heat flow within the workpiece by conduction as a chase for thermodynamical equilibrium, consequence of the thermal gradients. This phenomenon has been know as the law of heat conduction, also known as Fourier's law, and states that the time rate of heat transfer through a material is proportional to the negative gradient in the temperature and to the area at right angles, to that gradient, through which the heat is flowing [34, 47].

For a simple linear situation, where uniform temperature across equally sized elements exists, the heat flow rate between the elements is:

$$\frac{\Delta Q}{\Delta t} = -k \cdot A \frac{\Delta T}{\Delta x} \tag{5.8}$$

where ΔQ is the heat flow, Δt is the time interval, k is the thermal conductivity, A is the surface area of the element, ΔT is the temperature difference between the elements, and Δx is the length of the element. For each element, the total energy to be received/given is accounted with respect to all existing adjacent elements, one per face.

2.4.4. Phase and temperature determination

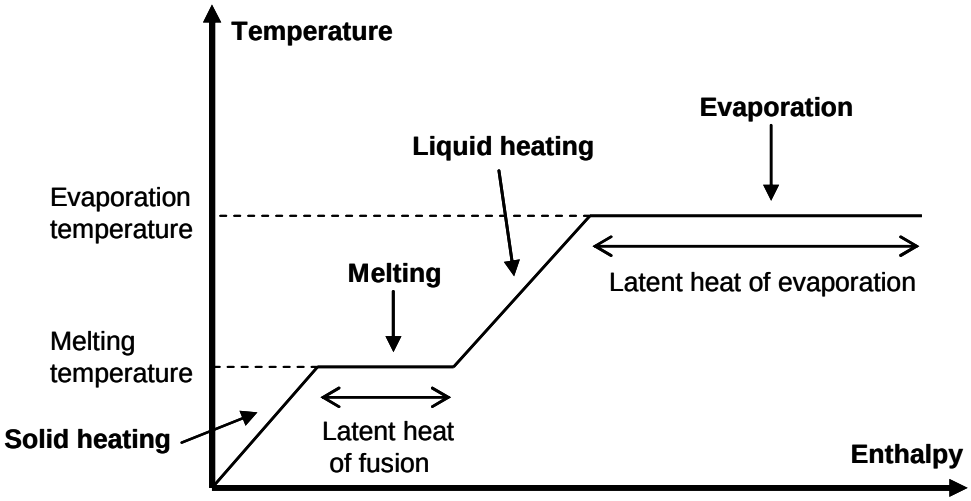

Fig. 5.7. Schematic diagram of the heating stages of the workpiece material during laser irradiation.

In Fig. 5.7 is illustrated a schematic diagram of the modeled material heating process assumed during laser irradiation. Four different stages and the consequent phases can be distinguished:

solid heating	-	solid phase
melting	-	solid + liquid phases
liquid heating	-	liquid phase
evaporation	-	liquid + gas phases

The whole process is governed by the enthalpy of the material, i.e. the energy per unit of mass. The boundaries of each stage are determined according the expression:

$$\frac{Q}{m} = Cp \cdot \Delta T \tag{5.9}$$

where Q is the heat energy of the element, m is the mass, Cp is the value of the specific heat capacity function (eq. 5.1) at the temperature limits of the stage, and ΔT is difference between the temperature limits of that stage and room temperature. Of course, the latent heats of fusion and/or evaporation have to be taken into account, if that is the case. Once identified the stage of the element, according to its enthalpy, the temperature is determined by rearranging the previous equation:

$$T = \frac{Q}{m \cdot Cp(T_{i-1})} + T_0 \tag{5.10}$$

where $Cp(T_{i-1})$ is the value of the specific heat capacity function (eq. 5.1) at the temperature of the previous iteration, and T_0 is the initial temperature, room temperature. This expression is applied only during solid and liquid phase heating. When the enthalpy of the material element is within the range of melting or evaporation it assumes the temperature of melting or evaporation, 2690°C or 4300°C, respectively.

2.4.5. Boundary conditions

The boundary condition assumed for the thermal analysis was an external layer at room temperature, 25°C, at each side and bottom. The objective of this is to provide escape of heat from the simulated workpiece, as it would be in a real (larger) workpiece sample. Otherwise, since the dimensions of the modeled workpiece are very small, the heat would be retained and the results would be adulterated.

2.4.6. Exportation of results

The resultant temperatures, energies and element mapping at the end of the run were exported into text files for data post-processing and for stress analysis. Moreover, temperature

profile maps were generated in autocad data exchange format (DXF) for ease of interpretation of the results. These maps were generated from the central cross-section XZ plane of the workpiece and a gradient of colors, from blue to red, was given to temperatures going from room temperature (25°C) to the evaporation temperature (4300°C). Also, phase maps were created from the same cross-section in order to simplify the identification of the different phase regions.

2.5. Description of the mechanical model

After the run with an incident laser beam, the resulting map of temperatures was exported to another program developed to calculate the thermal stresses in the workpiece. It was necessary to use a different method than that previously used for the thermal analysis. Instead of the finite difference method, in which there is a periodicity and unchanged shape/positioning of the elements/nodes, the finite element method (FEM) was found appropriate for this type of analysis.

Due to limitations concerning available CPU time and mainly RAM memory for simulation run, in this case it was not possible to perform a 3D approach, at least without optimization of the stiffness matrix storage and inversion method. The maximum allowed dimensions for the stiffness matrix was about 500 million elements which determined a 2D model with 200x100 elements ($(201x101)^2$ = 412.130.601 nodes). Since the modeling was only possible at 2D, each element was assumed as a 4-node square element. The axial stresses were calculated on the central-most XZ cross-cut of the sample.

Due to the exchange of method from finite difference to finite element and due to the need to work with nodes instead of single elements for the mechanical analysis it was necessary to assign a temperature to each node. For that, the temperature of each node was determined by averaging the temperature of the elements sharing that node. This is valid since we are considering an isotropic material and in which every element has equal dimensions.

The mechanical analysis was based on an elastic approach in which the goal consisted on determining stress distribution within the workpiece at a given moment in one single run. A flowchart diagram with the details of the procedures is illustrated in Fig 5.8. The main steps were:

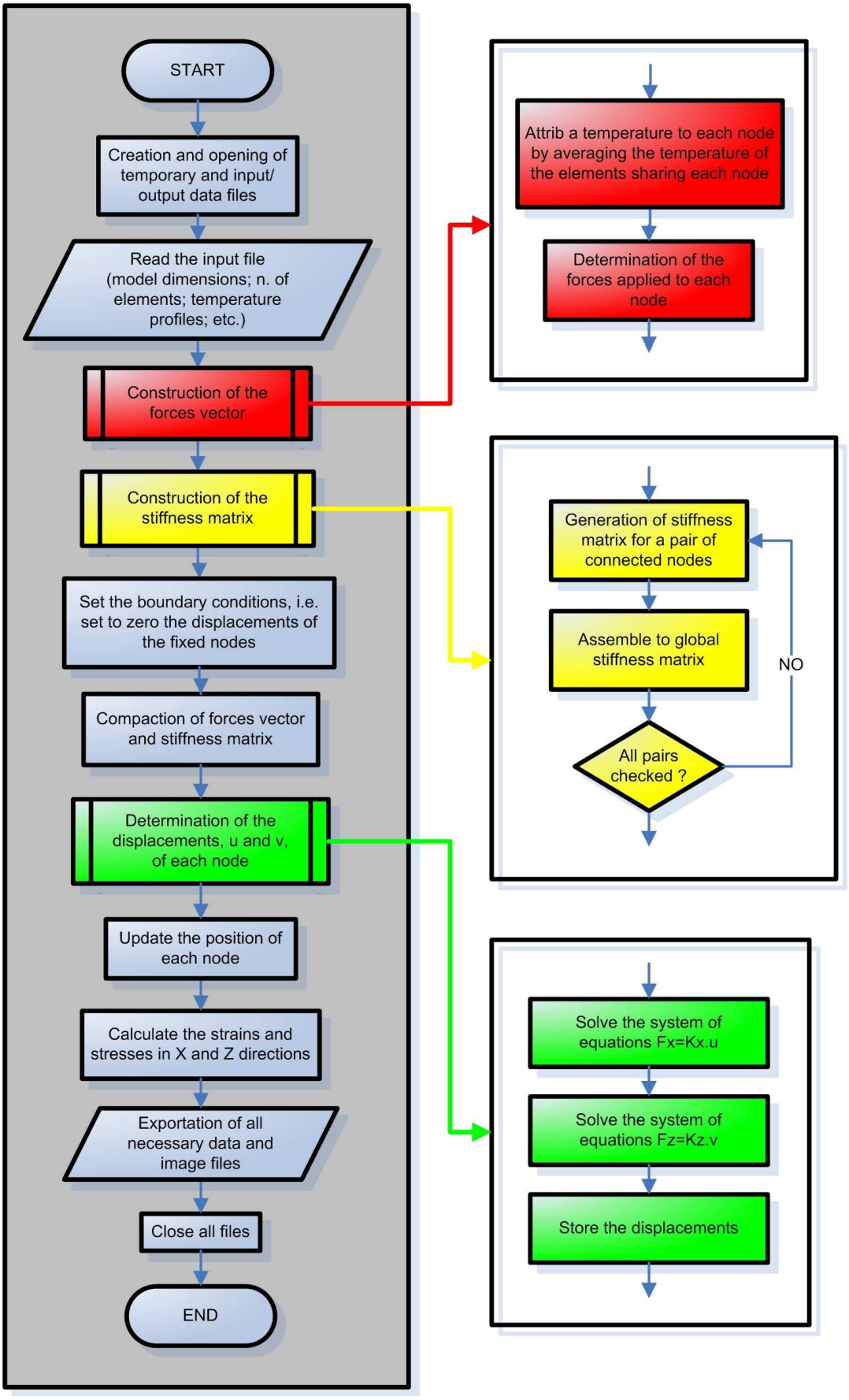

Fig 5.8. Flowchart diagram of the model approach used to perform the mechanical analysis.

- determination of the forces applied to each node
- assemblage of the stiffness matrix with the structural relationship of the nodes
- apply boundary conditions by setting to zero the displacement of the fixed nodes
- determination of the displacement of each node by solving the system of equations F=Ku
- determination of strains and stresses

2.5.1. Determination of forces

The forces applied to each node were determined from the Kingery's equation of thermal stress generated by a thermal gradient, given by [48]:

$$\sigma = \frac{E.\alpha.\Delta T}{1-\nu} \tag{5.11}$$

where σ is the stress; E the Young's modulus of elasticity; α the thermal expansion coefficient; ν the Poisson's ratio; ΔT difference between the actual temperature of the node and the room temperature.

$$\text{Since } \sigma = \frac{F}{A} \tag{5.12}$$

$$\text{then } F = \frac{E.\alpha.\Delta T.L^2}{1-\nu} \tag{5.13}$$

being F the force applied to the node and A or L^2 the area of the face of the element.

Each element will expand according to its own temperature, therefore the final F value applied to each node is the summation of the forces generated by the elements that share that node, as illustrated in Fig 5.9.

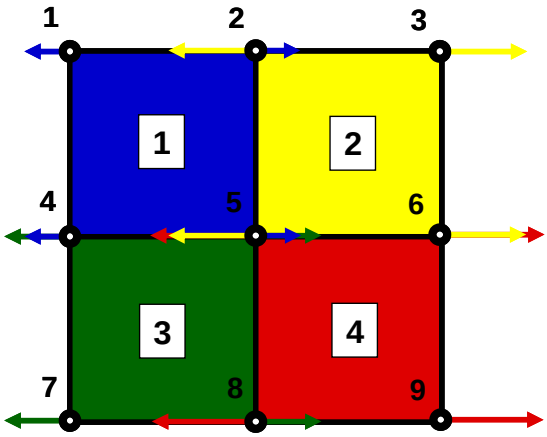

Fig 5.9. Schematic illustration of the determination of the forces applied to each node by the finite element method in a model of 2x2 elements and 3x3 nodes. This example shows only the forces applied in the horizontal (X) direction in a two-dimensional approach.

The next step was to store all forces in a vector (one-dimensional array), F, with the correspondence to the respective node:

$$F_x = \begin{Bmatrix} F_{x1} \\ F_{x2} \\ F_{x3} \\ F_{x4} \\ F_{x5} \\ F_{x6} \\ F_{x7} \\ F_{x8} \\ F_{x9} \end{Bmatrix} \tag{5.14}$$

2.5.2. Construction of the stiffness matrix

As shown in Fig 5.9, this example is a model with 4 elements (2 x 2) comprising 9 nodes (2+1 x 2+1). The numbering of each node according to its position in the 3X3 matrix is determined by the function:

$$\text{node} = i + (k-1) \times (Ni) \tag{5.15}$$

where *i* is the column position in the matrix, *k* is the row position in the matrix, and *Ni* is the total number of columns of the matrix.

A single stiffness matrix must be created for every pair of connected nodes of the existing elements. Then, all stiffness matrices are assembled in a global matrix comprising the information of the whole system:

$$K_x = \frac{E \cdot A}{L} \begin{bmatrix} k_{12}+k_{14} & -k_{12} & 0 & -k_{14} & 0 & 0 & 0 & 0 & 0 \\ -k_{12} & \dots & \dots & \dots & \dots & \dots & \dots & \dots & 0 \\ 0 & \dots & \dots & \dots & \dots & \dots & \dots & \dots & 0 \\ -k_{14} & \dots & \dots & .. & \dots & \dots & \dots & \dots & 0 \\ 0 & \dots & \dots & \dots & \dots & \dots & \dots & \dots & 0 \\ 0 & \dots & \dots & \dots & \dots & \dots & \dots & \dots & -k_{69} \\ 0 & \dots & \dots & \dots & \dots & \dots & \dots & \dots & 0 \\ 0 & \dots & \dots & \dots & \dots & \dots & \dots & \dots & -k_{89} \\ 0 & 0 & 0 & 0 & 0 & -k_{69} & 0 & -k_{89} & k_{89}+k_{69} \end{bmatrix}$$

where *L* is the cubic element side length, *A* is the element area and E is Young modulus. The K_{ab} have value 1 if the pair of nodes belong to the same direction of that of the stress to be determined and 1/L if perpendicular. In this particular example is represented part (filled only positions with respect to node 1 and 9) of the global stiffness in the X direction.

2.5.3. Assumptions and Boundary conditions

For the thermomechanical analysis we have set the boundary conditions as:

- nodes at the bottom and side of the modeled workpiece – fixed (displacement = 0)
- remaining nodes – free
- the material is considered to be in a initial stress-free state

Considering the example given in Fig 5.9 the u vector would be:

$$u = \begin{Bmatrix} 0 \\ u_2 \\ 0 \\ 0 \\ u_5 \\ 0 \\ 0 \\ 0 \\ 0 \end{Bmatrix} \tag{5.17}$$

2.5.4. Finding the solution

The solution to the system of equations (approximately 20000 for each direction, X and Z) F=K.u was achieved using the Gaussian elimination with partial pivoting method. An external subroutine [49] was used with some changes according the needs.

2.5.5. Determination of strains and stresses

When a body undergoes deformation under the action of external load and temperature distributions, the element OACB also deforms to the shape O'A'C'B' as shown in Fig 5.10.

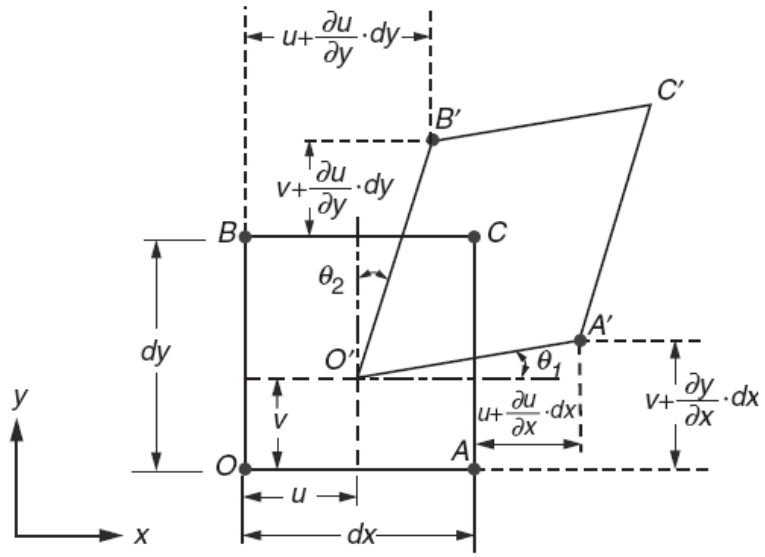

Fig 5.10. Deformation of a small element OACB [34].

The deformed shape of an elastic body under any given system of loads and temperature distribution conditions can be completely described by the two components of displacement u and v (in a 2d approach) parallel to the directions x and y, respectively. The strains induced in the body can be expressed in terms of the displacements u and v.

The normal strains ε_{xx} and ε_{yy} are calculated by dividing the change in length by the original length, for every segment:

$$\varepsilon_{yy} = \frac{\text{change in length of segment OB that lies in the y direction before deformation}}{\text{original length of segment OB}} \tag{5.18}$$

The stresses are then determined according the Hook's law:

$$\sigma_{yy} = E \cdot \varepsilon_{yy} \tag{5.19}$$

where E is the Young's modulus.

2.5.6. Exportation of results

The resulting data: node new positions, axial strain and stresses have been exported into text files so the information could be analyzed in detail later on.

3. Results

3.1. Thermal analysis

In the thermal analysis, the use of temperature dependent properties, such as specific heat capacity (Cp) and thermal conductivity (k), were evaluated by comparison with constant, temperature independent ones. Moreover, it has been studied the influence of the material's absorption coefficient, porosity level and laser beam spot radius. These analyses have been carried out by using the temperature-dependent properties. Since the measurements of the

absorption coefficient resulted in a wide range from 20000 to 50000 m^{-1}, the lack of accuracy in this parameter could have a significant influence in the final results. Both limits, 20000 and 50000, and an intermediate value, 35000m^{-1} have been tested. Regarding the porosity, its role on the heat conduction is known to be fundamental in a plasma-sprayed morphology. Since the porosity level in plasma-sprayed thermal barrier coatings is in the range of 5 - 20% [50-52], for the analysis, three different levels have been chosen: bulk (0%), 10% and 20%. The laser beam radius was also chosen to be varied since small variations have a great impact in the maximum power intensity, as described by eq. 5.4. The chosen beam radius were 0.215, as measured experimentally [3], 0.162 (2/3 of the measured radius) and 0.108mm (1/2 of the measured radius).

3.1.1. Influence of temperature dependent properties

In Table 5.3 are presented the parameters chosen for the analysis and the respective sample code. In bold are highlighted the varied parameters.

Table 5.3. Parameters used in the run.

Workpiece code	#1	#2
Absorption coefficient (m-1)	35000	35000
Porosity (%)	10	10
Beam radius (mm)	0.215	0.215
Heat capacity (J/(Kg.ºC))	**450 [53]**	**Eq. 5.1**
Thermal conductivity (W/(m.ºC))	**2.2 [39, 53]**	**Eq. 5.2**

In Fig. 5.11 and Fig 5.12 are illustrated the transient temperature distribution within the workpieces #1 and #2, respectively, for different times of the laser irradiation process. When compared to the images obtained for the material with temperature dependent properties it can be seen a remarkable difference in the eroded profiles. The huge difference is a result of the different heating rates and consequently in the evaporation rates. The temperature-dependent heat capacity (Cp) which increases with the increase in temperature, as seen in Fig 5.4, allow the material to require more energy to keep elevating its temperature as compared with the constant one.

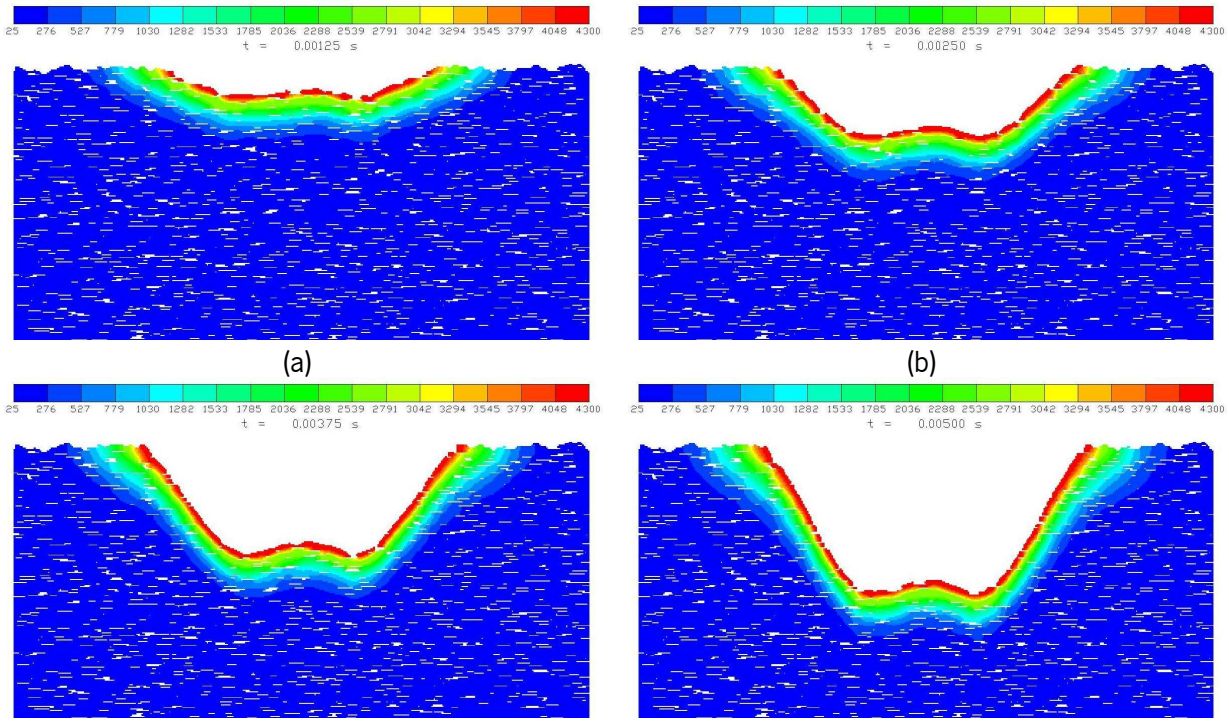

Fig. 5.11. Temperature distribution within workpiece #1 during laser irradiation: (a) 125ms; (b) 250ms; (c) 375ms; (d) 500ms.

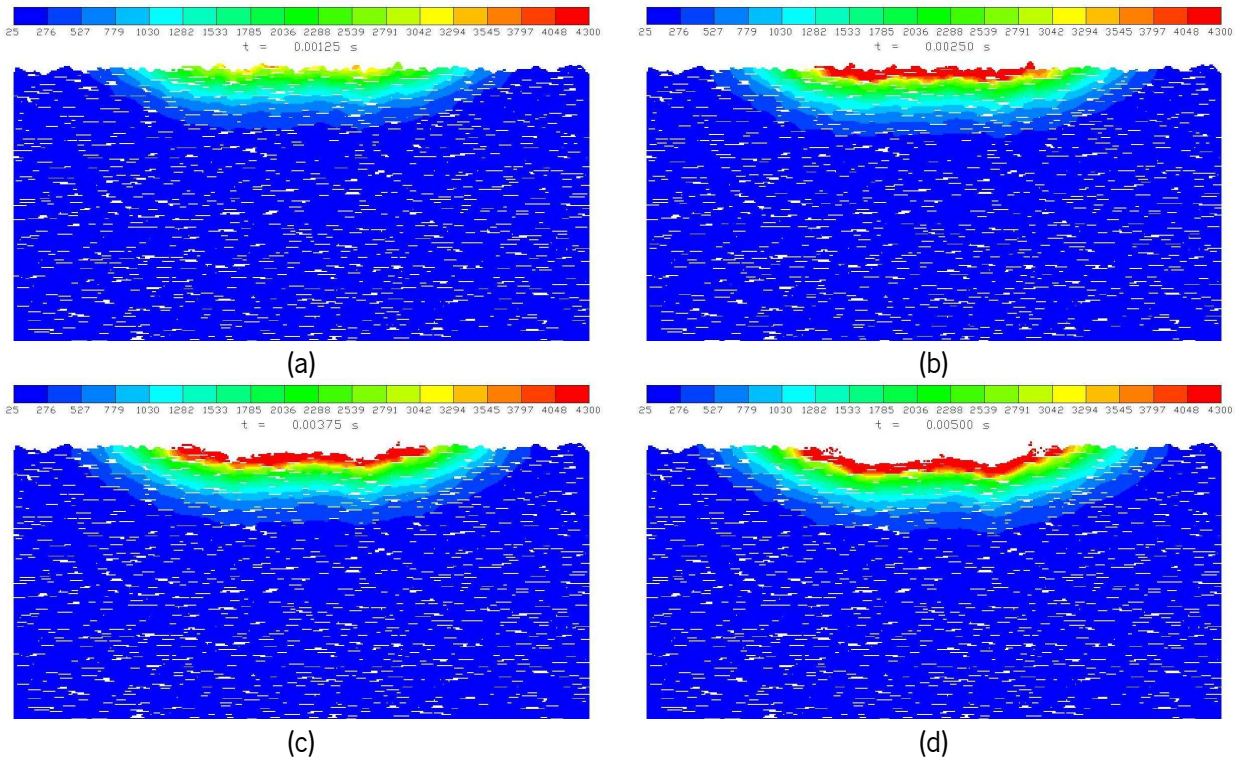

Fig 5.12. Temperature distribution within workpiece #2 during laser irradiation: (a) 125ms; (b) 250ms; (c) 375ms; (d) 500ms.

Moreover, the temperature-dependent thermal conductivity (k) also contributes to increase the dissipation of energy from the warmer regions to the colder ones, allowing the material to take a longer time to evaporate.

Phase distribution images, immediately at the end of laser irradiation, depicted in Fig. 5.13, show the location and dimensions of each phase. A remarkable difference is observed for the two molten profiles.

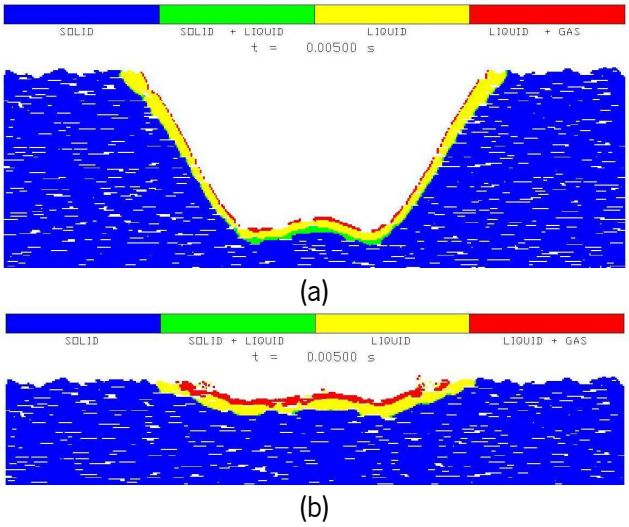

Fig. 5.13. Phase distribution within workpiece #1 (a), and #2 (b) at the end of the run (500ms).

The exported data used to the generation of the images previously presented allowed a detailed numerical analysis to determine the thickness and width of the molten layers. In Fig. 5.14 are presented the widths of the molten layers obtained for the two types of properties. They were determined from the difference in distance between the molten elements located most far from the center, for each sample. The obtained molten layer widths were 934 μm for the simulation with constant properties and 772 μm for the simulation with temperature-dependent properties.

The molten layer thicknesses have also been determined and are presented in Fig. 5.15. The molten layer thicknesses have been determined by calculating the depth at each point of the layer width in X. Therefore, the presented results refer to minimum, maximum and average, for each sample.

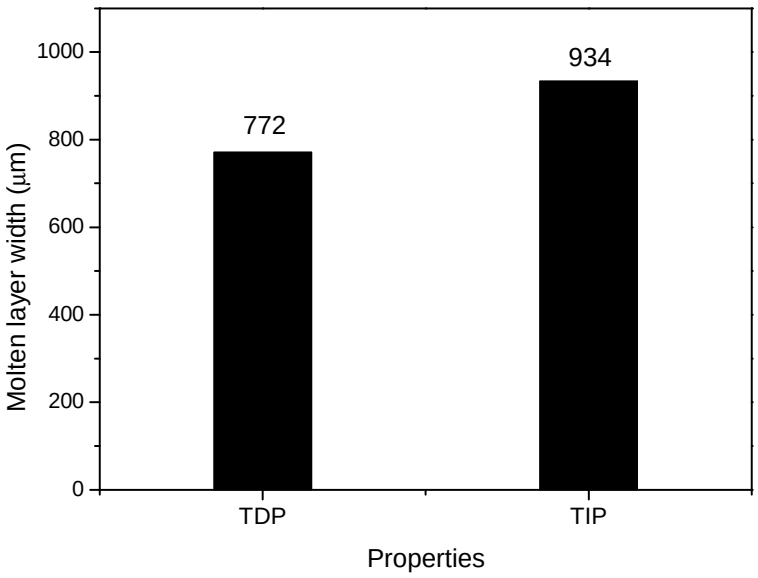

Fig. 5.14. Comparison of the molten track widths obtained for the different type of properties: TDP - temperature-dependent properties; TIP – temperature-independent-properties.

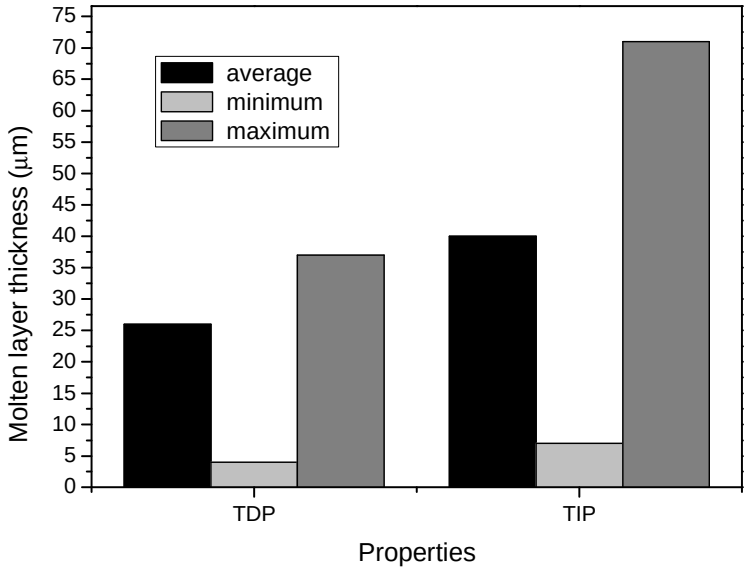

Fig. 5.15. Comparison of the molten track thicknesses obtained for the different type of properties: TDP - temperature-dependent properties; TIP – temperature-independent-properties.

A temperature profile plotted along Z (depth) at the central-most section of the workpiece has been drawn for each sample and is shown in Fig. 5.16. Although the curve obtained with constant properties is shifted to the right, due to the higher evaporation, the drop in temperature

is quite similar. In order to better observe the differences in temperature along Z, one curve was subtracted to the other and the difference is plotted in Fig. 5.17. As it can be seen, regardless the differences in evaporated profiles, there are temperature differences reaching about 700°C, considering both surfaces at the same height.

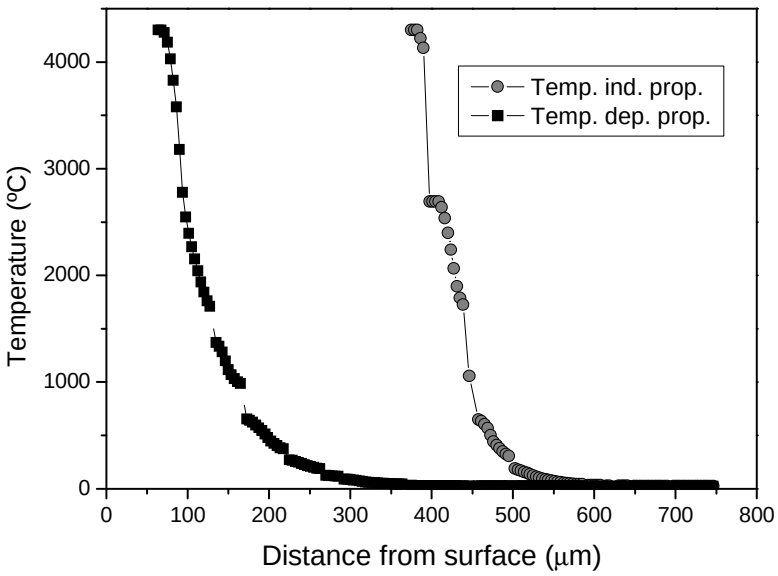

Fig. 5.16. Comparison of the temperature distribution along Z direction at the central most section of the shown images. The curves refer to the two different types of properties.

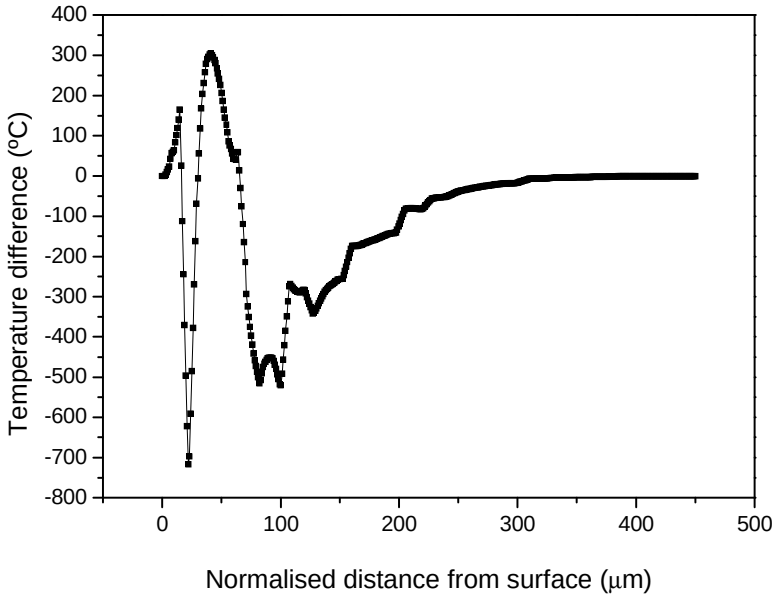

Fig. 5.17. Difference in temperature, along Z, between the profiles obtained for temperature dependent and independent properties.

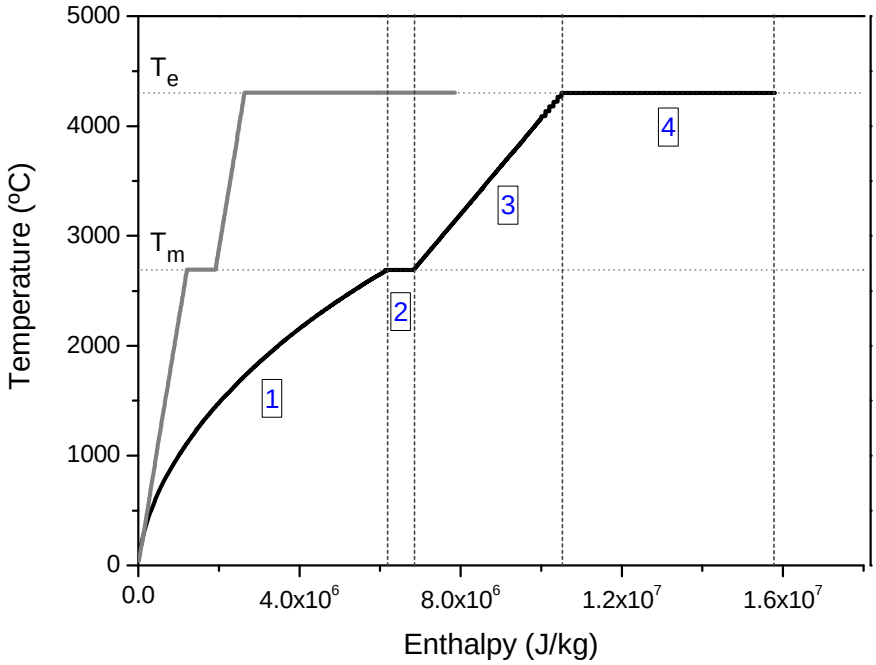

Fig 5.18. Calculated temperature evolution of a single element during the laser irradiation. The black curve refers to an element with temperature dependent properties while the grey refers to an element with constant properties.

In Fig 5.18 are plotted the temperature evolution of two elements of the surface which have been through all the stages of the heating process and finally evaporated. The black curve refers to an element with temperature-dependent properties described by eqs. 5.1 and 5.2, for specific heat and thermal conductivity, respectively. For comparison, is shown in grey, the evolution of the same element but with constant, temperature independent specific heat capacity and thermal conductivity. There can be seen four distinct regions. In the first region a faster heating during the initial period is owed to the low specific heat at lower temperatures, given by eq. 5.1. When the melting temperature is reached the element does not heat up anymore until all the required heat of fusion has been absorbed. Again, the element heats up, but linearly due to the constant specific heat assumed above the melting point. At last, when reaching the evaporation temperature, the element absorbs all the heat of evaporation and is finally evaporated. Comparing both curves, It can be seen a great difference, specially during the first stage which is owed to the temperature dependent specific heat, responsible for requiring increasing amounts of heat to continue elevating its temperature. For the whole process, the temperature dependent element required to evaporate about twice the energy density of that of the constant properties element, 1.58×10^7 and 7.85×10^6 J/(kg.°C), respectively.

In Fig. 5.19 is plotted the temperature evolution with time, for the same element located at the surface in the central-most region of the plane shown in the images. The differences in the heating rates for different properties type are evident. The element evaporated after 128.5 and 291.1 ms for temperature-independent and temperature-dependent properties, respectively. The estimated linear heating rates were 2441 and 1321°C/ms for temperature-independent and temperature-dependent properties, respectively.

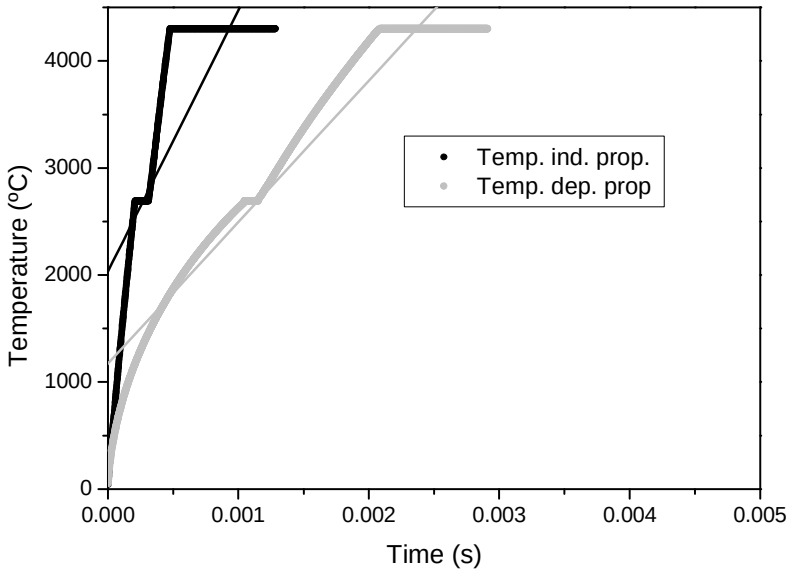

Fig. 5.19. Comparison of the temperature evolution with time of top-most element at the central-most section of the shown images. The straight lines represent the linear fitting for estimating the heating rates.

3.1.2. Influence of the absorption coefficient

For ease of referencing, in Table 5.4 are listed the parameters chosen for the analysis and the respective sample code. In bold are highlighted the varied parameters.

Table 5.4. Parameters used in the run.

Workpiece code	#3	#2	#4
Absorption coefficient (m^{-1})	**20000**	**35000**	**50000**
Porosity (%)	10	10	10
Beam radius (mm)	0.215	0.215	0.215

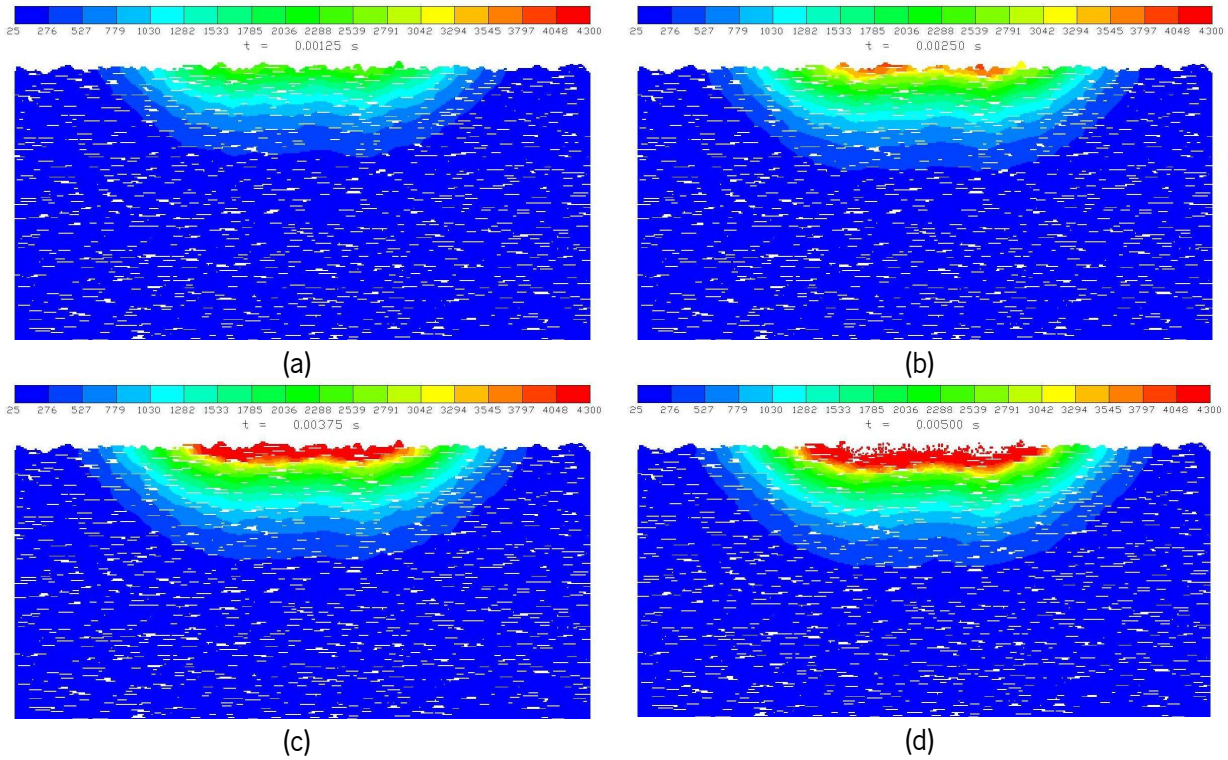

Fig 5.20. Temperature distribution within workpiece #3 during laser irradiation: (a) 125ms; (b) 250ms; (c) 375ms; (d) 500ms.

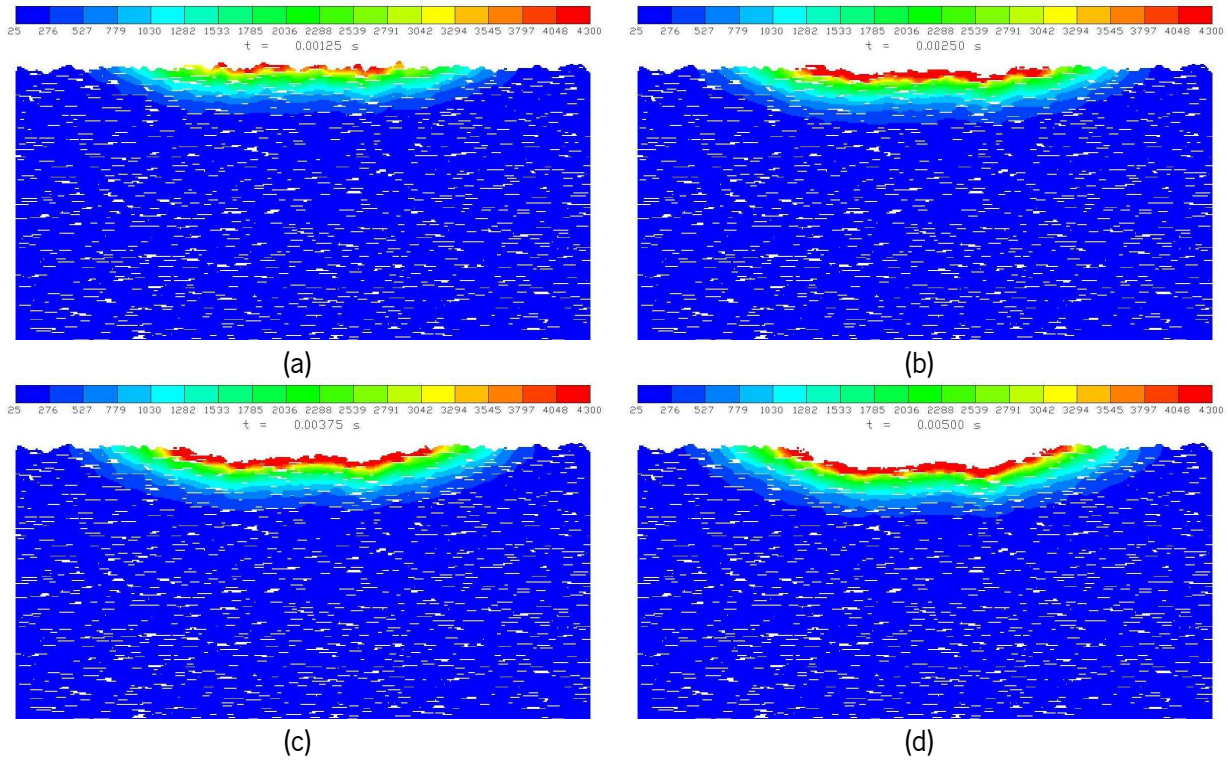

Fig 5.21. Temperature distribution within workpiece #4 during laser irradiation: (a) 125ms; (b) 250ms; (c) 375ms; (d) 500ms.

In Fig 5.20 and Fig 5.21 are illustrated the transient temperature distribution within the workpieces #3 and #4 respectively, for different times of the laser irradiation process. The temperature profile referring to workpiece #2 has been presented previously in Fig 5.12. The differences are evident. The lower the absorption coefficient is, a deeper penetration of the laser light will be allowed and therefore the total energy of the laser will be spread over a larger region within the material. Consequently, the energy received by each location (element) at the material will be lower and therefore the heating rate will also be lower. The surface profiles at the end of the simulation are considerably different as a result of the heating and evaporation rate of the material. It can be noticed that the surface profiles evidence the laser beam power intensity distribution seen in Fig 5.5.

Phase distribution images, immediately at the end of laser irradiation, depicted in Fig 5.22, show the location and dimensions of each phase. It can be seen that with an increase of the absorption coefficient the molten layer tends to be thinner but wider.

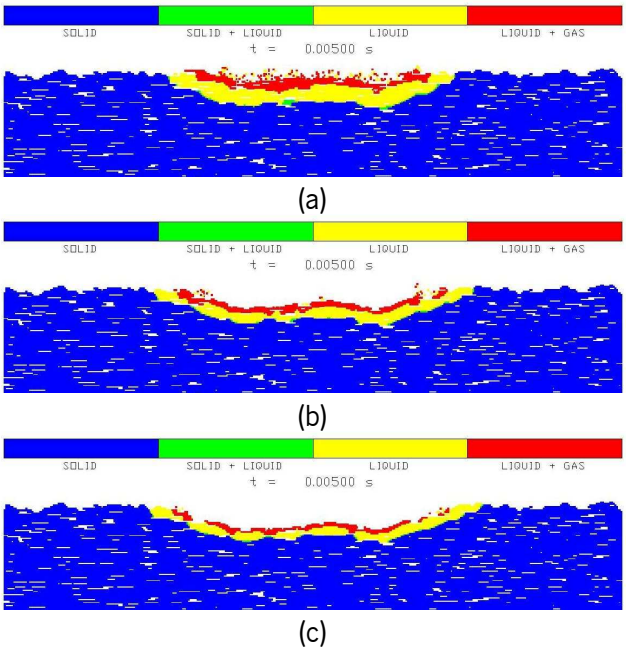

Fig 5.22. Phase distribution within workpiece #3 (a), #2 (b) and #4 (c) at the end of the run (500ms).

In Fig. 5.23 are presented the widths of the molten layers obtained for the different absorption coefficients. They were obtained from the difference of distance between the molten elements located most on the right and most on the left, for each sample. The obtained molten

layer widths were 694, 772 and 806 μm, for the absorption coefficients of 20000, 35000 and 50000 respectively. The molten layer thicknesses have also been determined and are presented in Fig. 5.24. As previously stated when referring to Fig 5.22, the increase of the absorption coefficient results in a decrease of the molten layer thickness and this is due to a lower penetration of the radiation which gives rise to a more concentrated distribution of the energy.

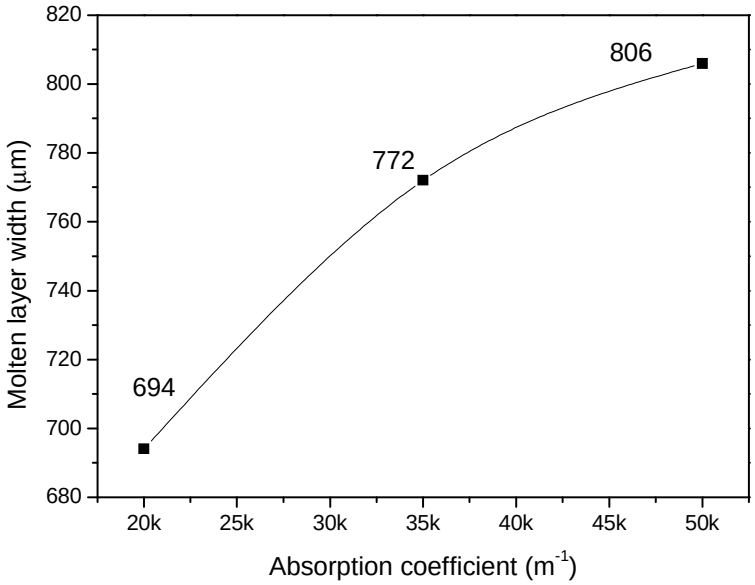

Fig. 5.23. Comparison of the track widths obtained for the three different absorption coefficients.

A temperature profile plotted along Z (depth) at the central-most section of the workpiece has been drawn for each sample and is shown in Fig 5.25. The differences in the drop of temperature along Z (depth) for the different absorption coefficients are evident. Since the temperatures near the surface reach higher values in a short period of time, for higher absorption coefficients, the material at the surface gets evaporated faster. This fact explains why the curves are shifted to the right at the very beginning, at or near the surface. However, since the heating is more pronounced near the surface, for higher absorption coefficients, the drop in temperature is higher as we go down in Z, as can be observed by the slope of the curves.

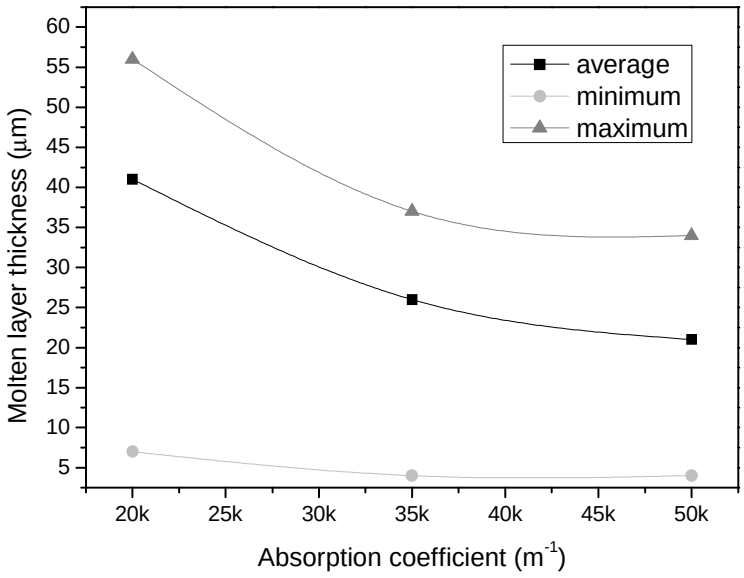

Fig. 5.24. Comparison of the molten track thicknesses obtained for the three different absorption coefficients.

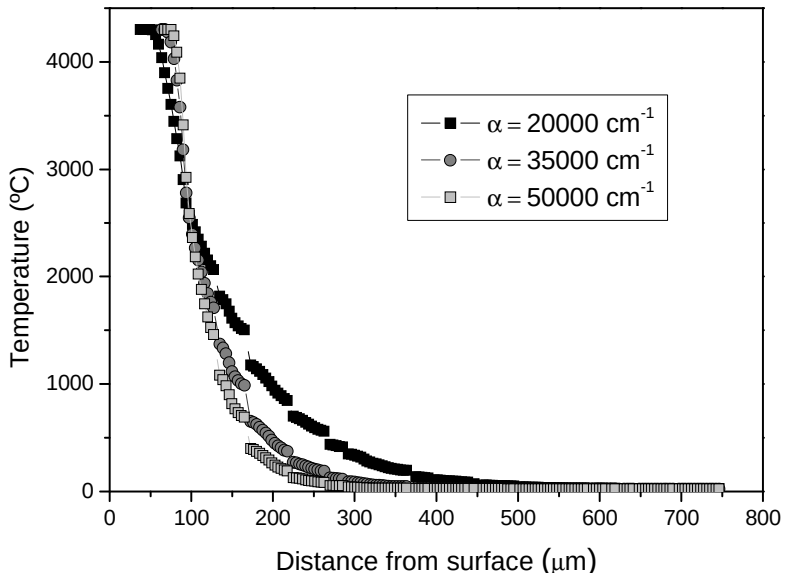

Fig 5.25. Comparison of the temperature distribution along Z direction at the central most-section of the shown images. The curves refer to the three different absorption coefficients.

The differences in temperature along Z (normalized means that the surface Z value is considered to the same for both), determined from the curves of α=20000 and 50000m^{-1}, shown in Fig 5.25 are plotted in Fig. 5.26. As it can be seen, this difference in the absorption coefficient resulted in a maximum temperature difference ranging 1400°C, very close to the surface.

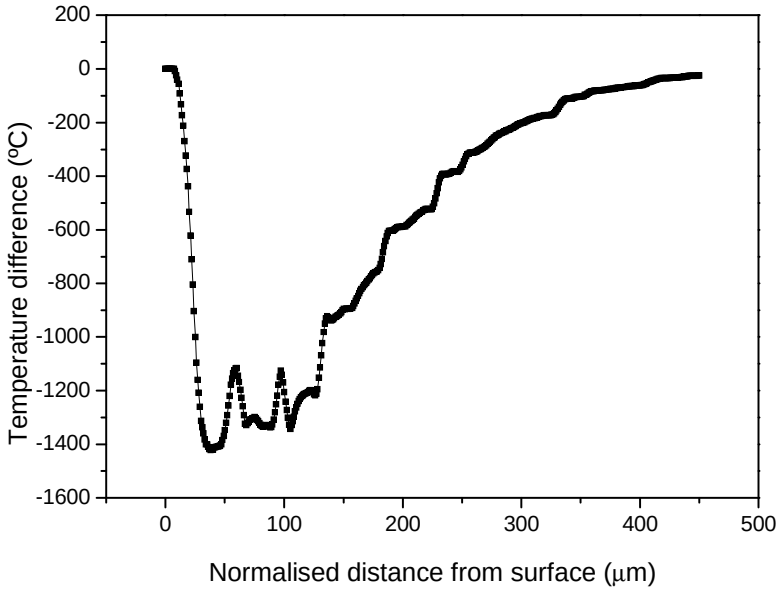

Fig. 5.26. Difference in temperature, along Z, between the profiles obtained for α=20000 and 50000m^{-1}.

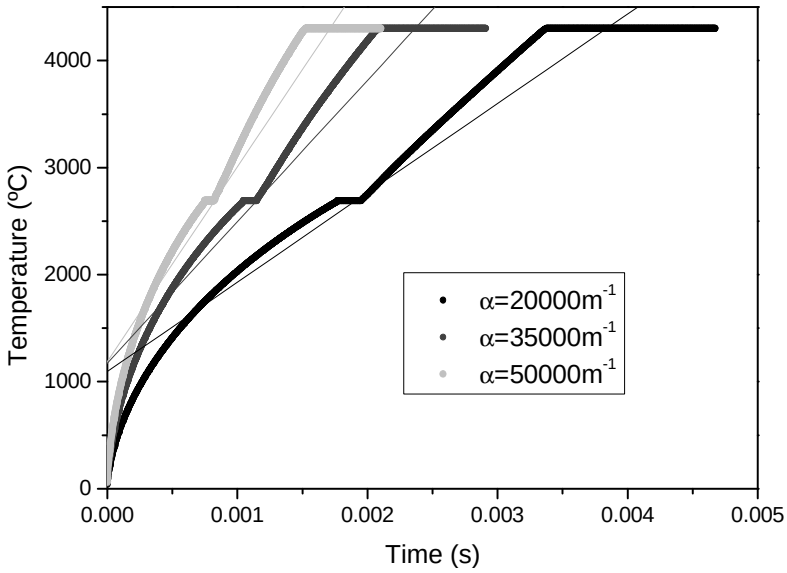

Fig. 5.27. Comparison of the temperature evolution with time of top-most element at the central-most section of the shown images. The straight lines represent the linear fitting for estimating the heating rates.

In Fig. 5.27 is plotted the temperature evolution with time, for the same element located at the surface in the central-most region of the plane shown in the images. It can be observed considerable differences in the heating rates depending on the absorption coefficients. The

element evaporated after 210.5, 291.1 and 467.5 ms for α=50000, 35000 and 20000m^{-1}, respectively. The estimated linear heating rates were 1818, 1321 and 835°C/ms for α=50000, 35000 and 20000m^{-1}, respectively.

3.1.3. Influence of porosity level

In Table 5.5 are presented the parameters chosen for the analysis and the respective sample code. In bold are highlighted the varied parameters.

Table 5.5. Parameters used in the run.

Workpiece code	#5	#2	#6
Absorption coefficient (m-1)	35000	35000	35000
Porosity (%)	**0**	**10**	**20**
Beam radius (mm)	0.215	0.215	0.215

In Fig 5.28 and Fig 5.29 are illustrated the transient temperature distribution within the workpieces #4 and #5 respectively, for different times of the laser irradiation process. The temperature profile referring to workpiece #2 has been presented previously in Fig 5.12. The evolution of temperature appears to be quite similar for all porosity levels. The obvious difference is the increasing irregularity of the evaporated surface as a result of the increase in porosity.

Phase distribution images shown in Fig. 5.30, show the location and dimensions of each phase. Unlike the previous results regarding the absorption coefficient, it can be seen that the differences with respect to molten layer thickness and width are not evident. However, it is clear that the molten layer becomes much more irregular with an increase of porosity. The inclusion of fluid flow by gravity, surface tension and thermocapilarity would certainly play an important role in the analysis of the influence of porosity. Obviously, the molten layer would flow and fill the voids densifying the material and reducing the roughness at the surface of that region.

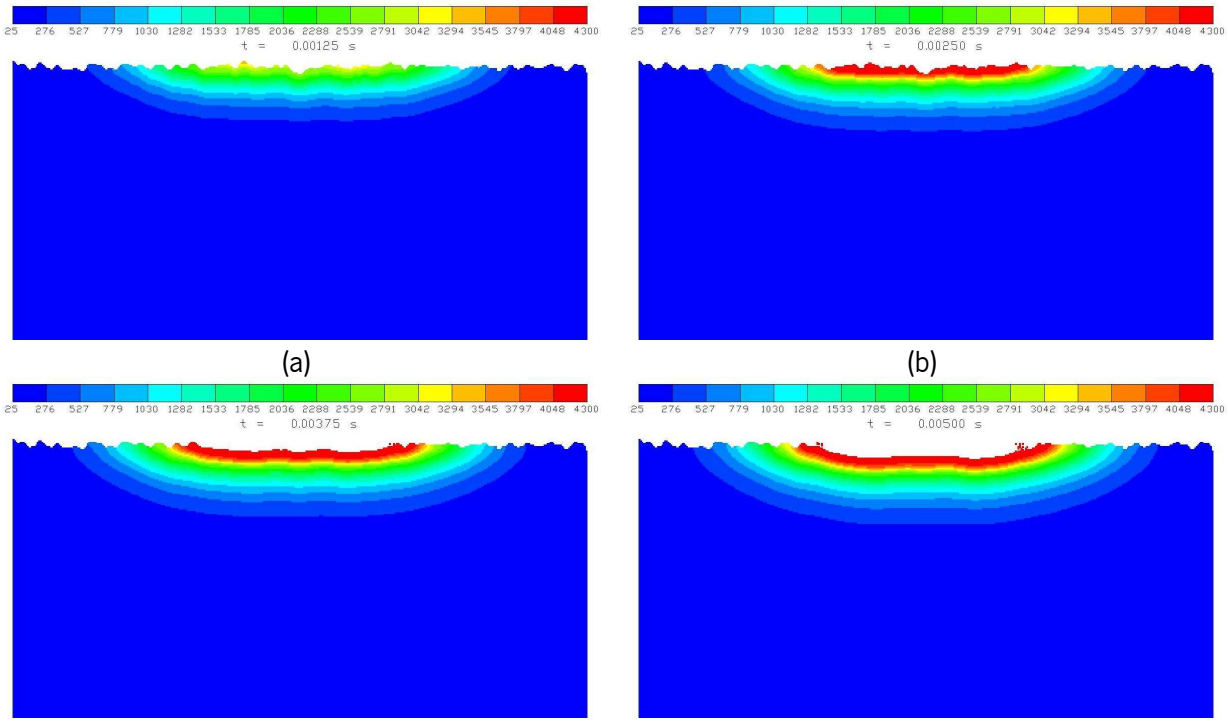

Fig 5.28. Temperature distribution within workpiece #5 during laser irradiation: (a) 125ms; (b) 250ms; (c) 375ms; (d) 500ms.

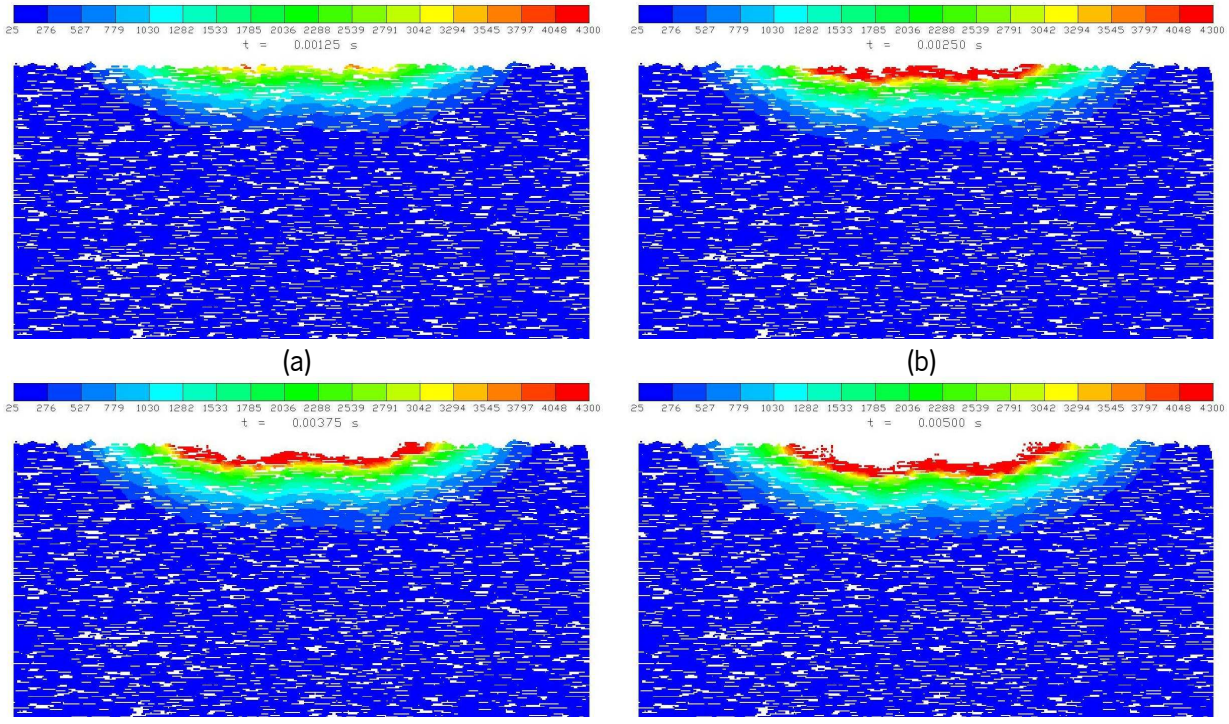

Fig 5.29. Temperature distribution within workpiece #6 during laser irradiation: (a) 125ms; (b) 250ms; (c) 375ms; (d) 500ms.

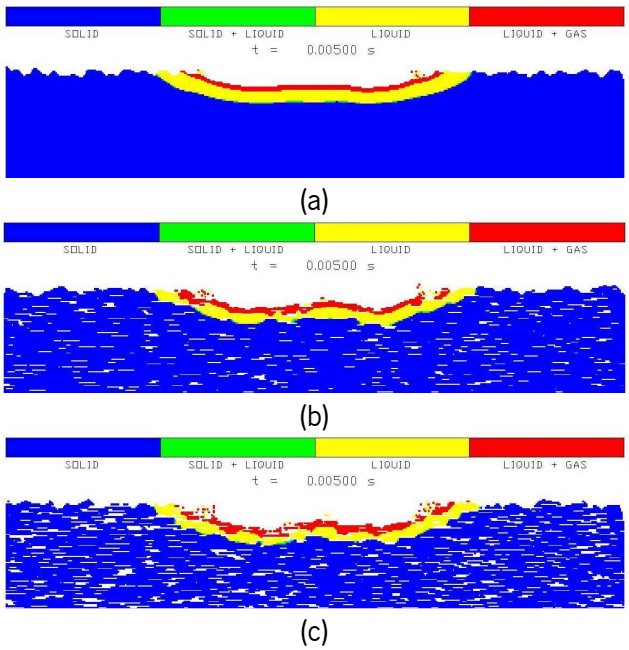

Fig. 5.30. Phase distribution within workpiece #5 (a), #2 (b) and #6 (c) at the end of the run (500ms).

In Fig. 5.31 are presented the widths of the molten layers obtained for the different absorption coefficients. The obtained molten layer widths were 761, 772 and 788 μm, for the porosity levels of 0, 10 and 20, respectively. The molten layer thicknesses have also been determined and are presented in Fig. 5.32. It can be observed that the thickness of the molten layer decreases with the increase of the porosity level. However, for the maximum values obtained, there is an opposite behavior when going from 10 to 20% porosity. This can be explained by the heat transfer by conduction being lower in depth due to the horizontal porosity. However, the higher the porosity the higher is the penetration of the laser beam into the material, and therefore the temperature is also higher for deeper depths. The balance of both contributions dictates the thickness of the molten layer.

A temperature profile plotted along Z (depth) at the central-most section of the workpiece is shown in Fig. 5.33, for the three different porosity levels. From the slope of the curves, the dissimilar drop in temperature along Z (depth) for the different porosities is observed. However, In this case, the difference is not much pronounced.

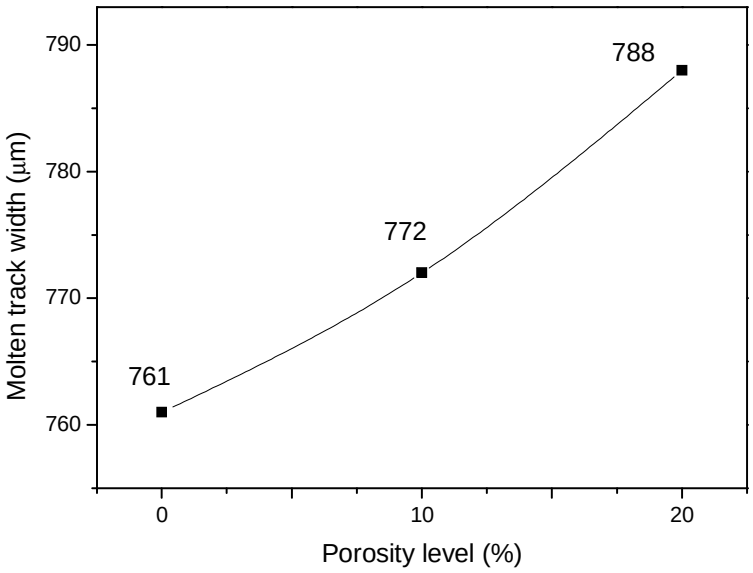

Fig. 5.31. Comparison of the track widths obtained for the three different porosity levels.

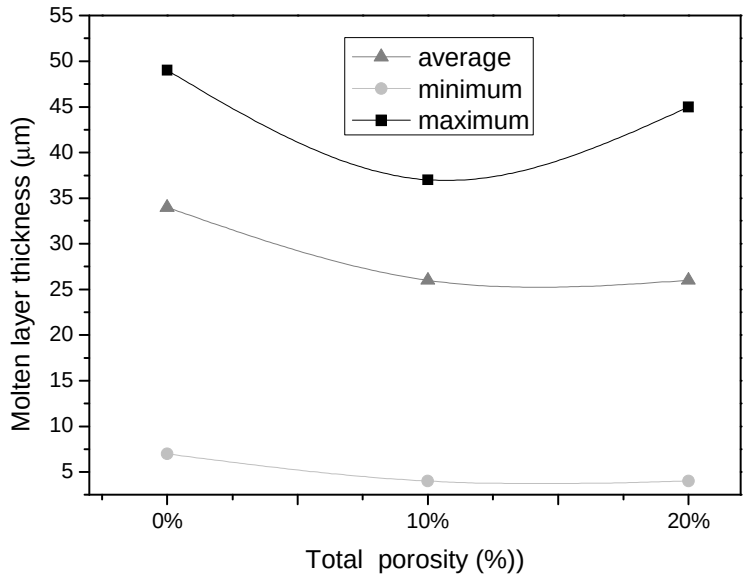

Fig. 5.32. Comparison of the molten track thicknesses obtained for the three different porosity levels.

The differences in temperature, determined from the curves with respect to porosity of 0 and and 20%, shown in Fig. 5.33 are plotted in Fig. 5.34. As it can be seen, this difference in the porosity level resulted in maximum temperature differences ranging 400-500°C, very close to the surface.

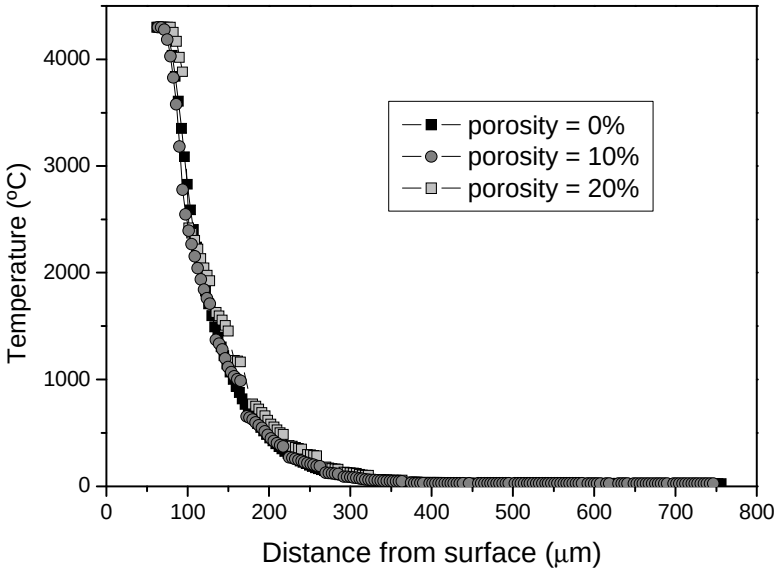

Fig. 5.33. Comparison of the temperature distribution along Z direction at the central most section of the shown images. The curves refer to the three different porosity levels.

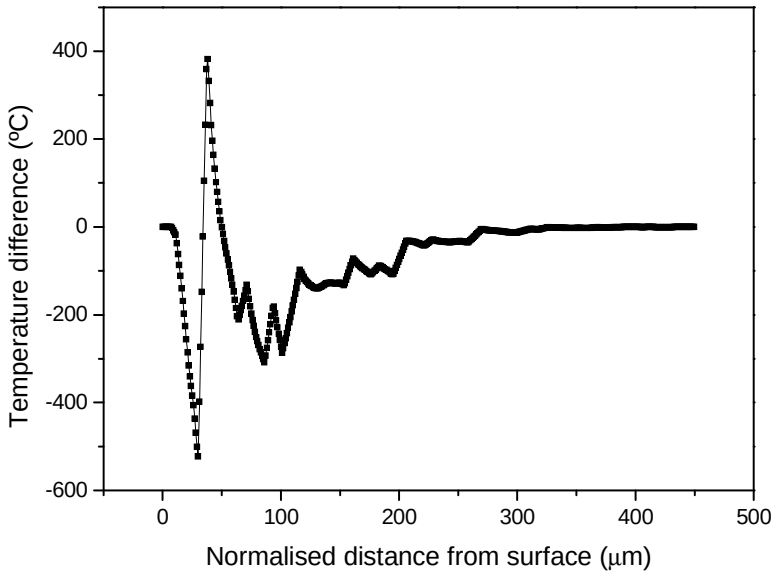

Fig. 5.34. Difference in temperature, along Z, between the profiles obtained for porosity=0 and 20%.

In Fig. 5.35 is plotted the temperature evolution with time, for the same element located at the surface in the central-most region of the plane shown in the images. The differences in the heating rates for different porosities are evident. The element evaporated after 265.2, 291.1 and 381.9 ms for porosity=20, 10 and 0%, respectively. The estimated linear heating rates were 1488, 1321 and 975°C/ms for porosity=20, 10 and 0%, respectively.

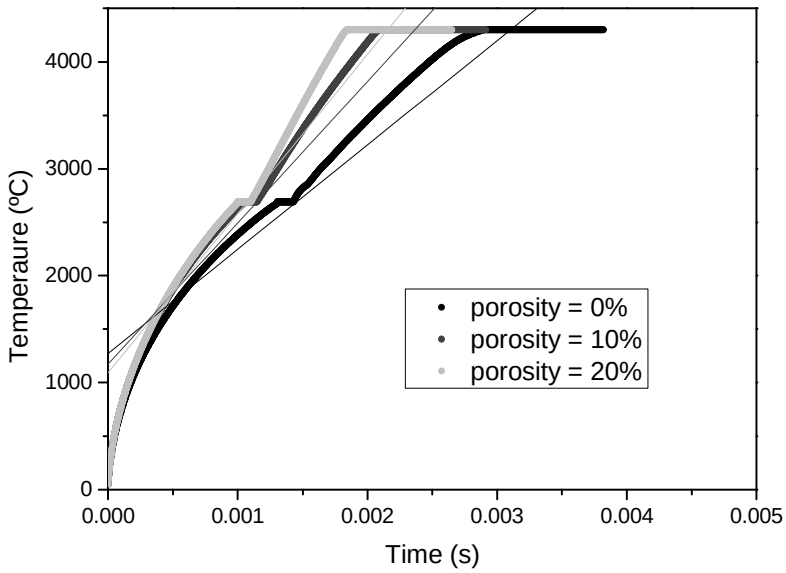

Fig. 5.35. Comparison of the temperature evolution with time of top-most element at the central-most section of the shown images. The straight lines represent the linear fitting for estimating the heating rates.

3.1.4. Influence of laser beam spot size

In Table 5.6 are presented the parameters chosen for the analysis and the respective sample code. In bold are highlighted the varied parameters.

Table 5.6. Parameters used in the run.

Workpiece code	#7	#8	#2
Absorption coefficient (m-1)	35000	35000	35000
Porosity (%)	10	10	10
Beam radius (mm)	**0.108**	**0.162**	**0.215**

In Fig 5.36 and Fig 5.37 are illustrated the transient temperature distribution within the workpieces #7 and #8 respectively, for different times of the laser irradiation process. The temperature profile referring to workpiece #2 has been presented previously in Fig 5.12. As it can be observed, the laser beam radius has a significant influence in the heating rate of the material. Being the laser power constant, if reducing the beam size (focusing) at the surface of the material the power density increases considerably according to eq. 5.4. Therefore, the high heating rate allows the material to get through all heating stages and be evaporated much faster.

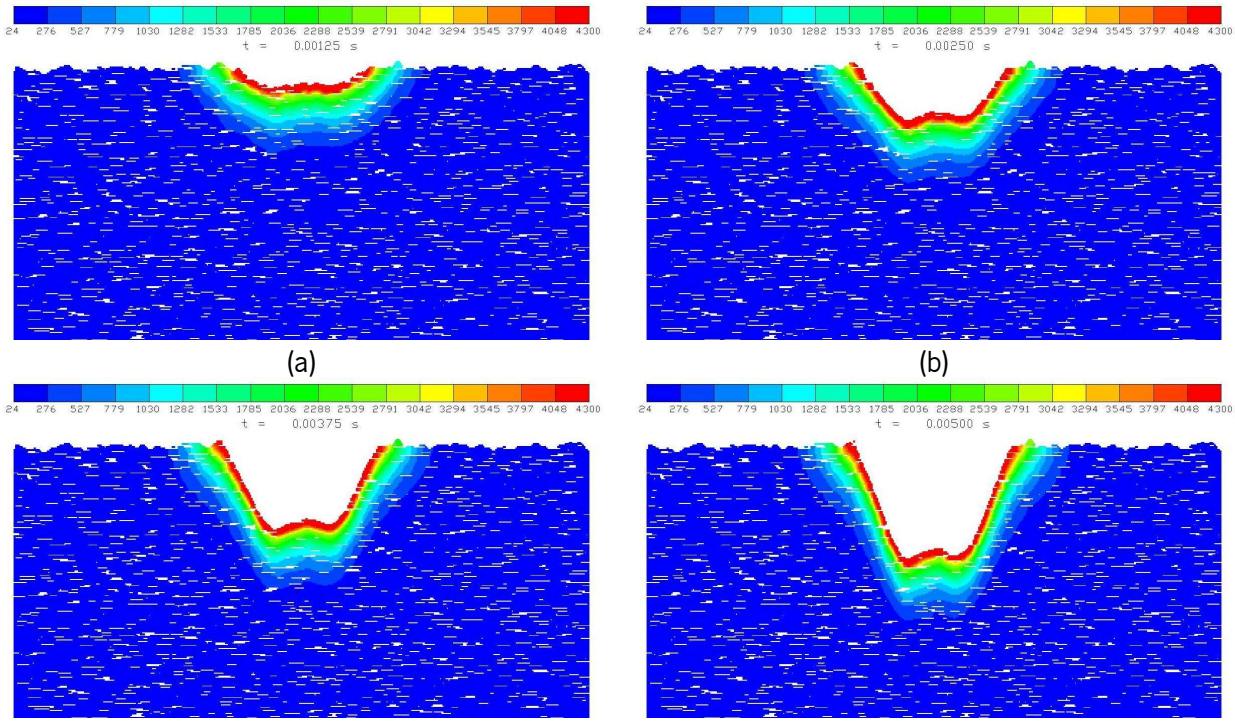

Fig 5.36. Temperature distribution within workpiece #7 during laser irradiation: (a) 125ms; (b) 250ms; (c) 375ms; (d) 500ms.

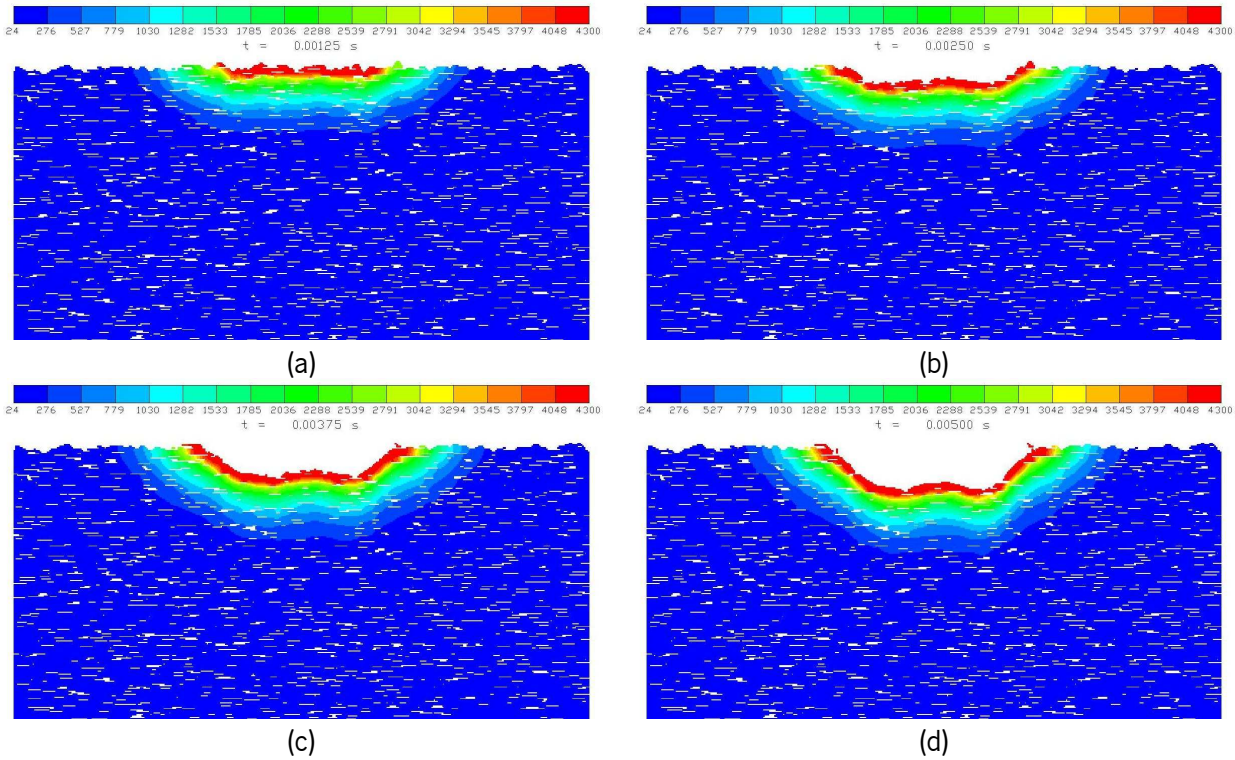

Fig 5.37. Temperature distribution within workpiece #8 during laser irradiation: (a) 125ms; (b) 250ms; (c) 375ms; (d) 500ms.

Phase distribution images shown in Fig. 5.38, show the location and dimensions of each phase. Obviously, in this case, the differences with respect to molten layer width were already expected to be larger for larger beam radius. In Fig. 5.39 are presented the widths of the molten layers obtained for the different laser beam radius. The obtained molten layer widths were 488, 664 and 772 μm, for the beam radius of 0.108, 0.162 and 0.215, respectively. Concerning to the molten layer thickness, the calculated values shown in Fig. 5.40 reveal a decrease when increasing the beam radius. However, when observing the phase images shown in Fig. 5.38 they suggest the opposite. In fact, the calculation of the thickness is based on the maximum distance, in the vertical direction (Z), between two molten elements. Since the slope of the molten profile is very high, due to large quantity of material vaporized, the calculation is not very effective. Instead, the calculation should be accurate if measuring the thickness perpendicularly to the profile.

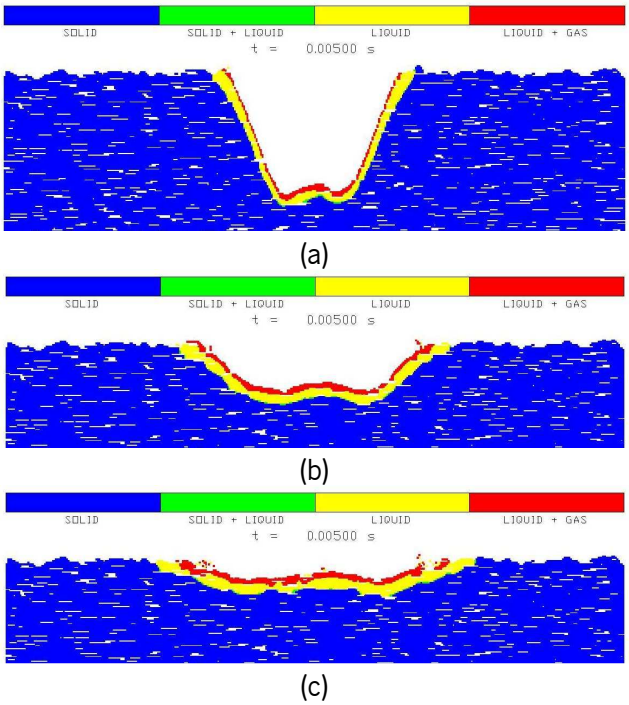

Fig. 5.38. Phase distribution within workpiece #7(a), #8 (b) and #2 (c) at the end of the run (500ms).

A temperature profile plotted along Z (depth) at the central-most section of the workpiece is shown in Fig. 5.41, for the three different laser beam radius. It can be seen an increasing shift to higher depths for lower beam radius. This is due to the high heating hate which evaporates the material much faster. Concerning to the shape of curves they appear to be very similar. In order to better observe the differences in temperature along Z, the curve referring to the large radius

was subtracted to the curve referring to the smaller radius (Fig. 5.42). As it can be seen, the laser beam radii difference resulted in maximum temperature differences ranging 750°C.

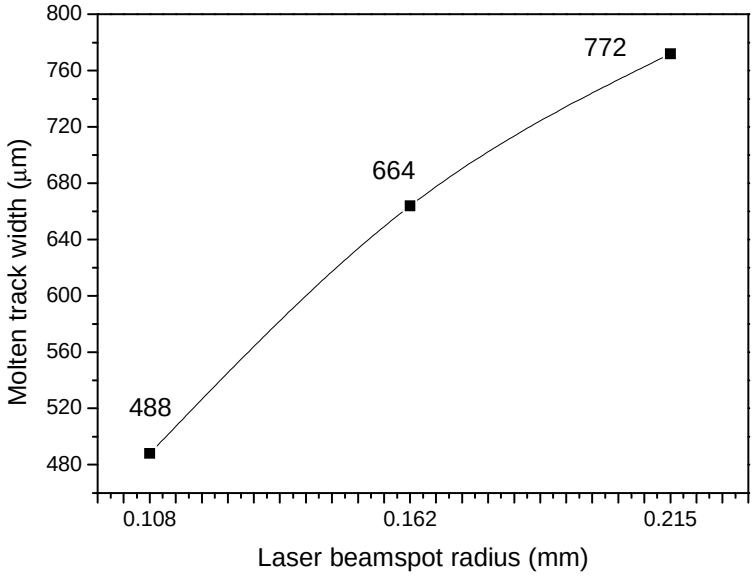

Fig. 5.39. Comparison of the molten track widths obtained for the three different laser beam spot radius.

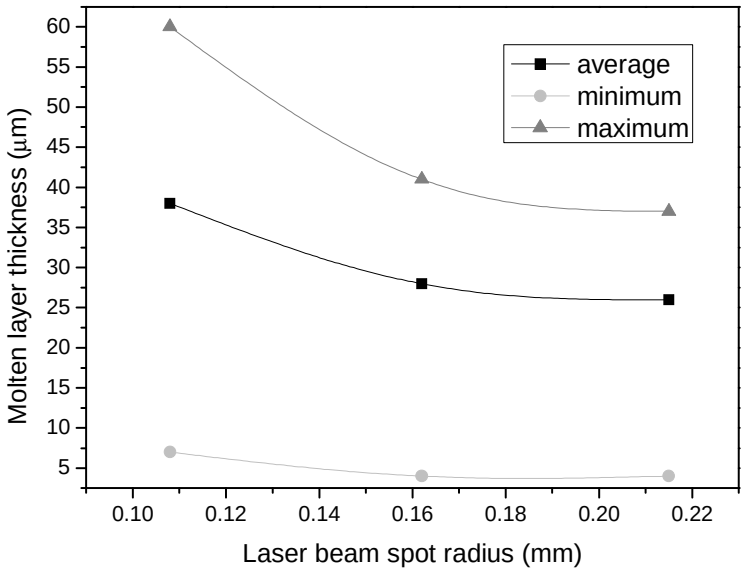

Fig. 5.40. Comparison of the molten track thicknesses obtained for the three different laser beam spot radius.

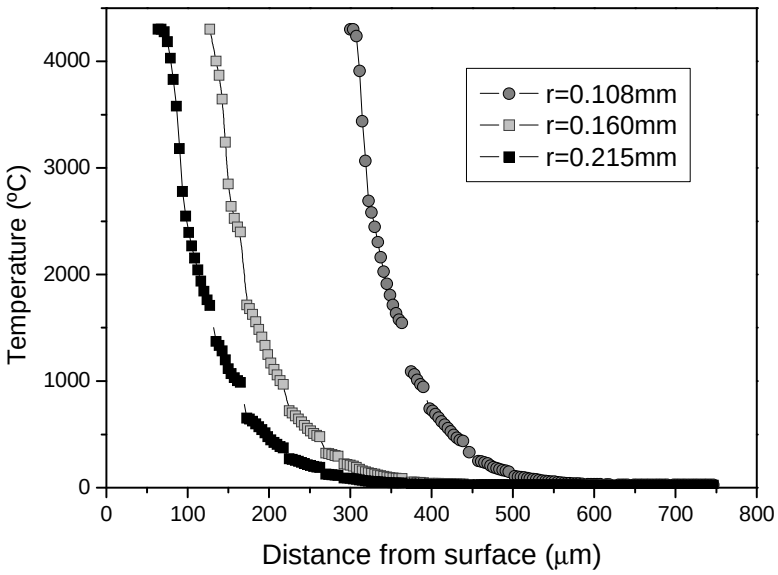

Fig. 5.41. Comparison of the temperature distribution along Z direction at the central most section of the shown images. The curves refer to the three different beam radius.

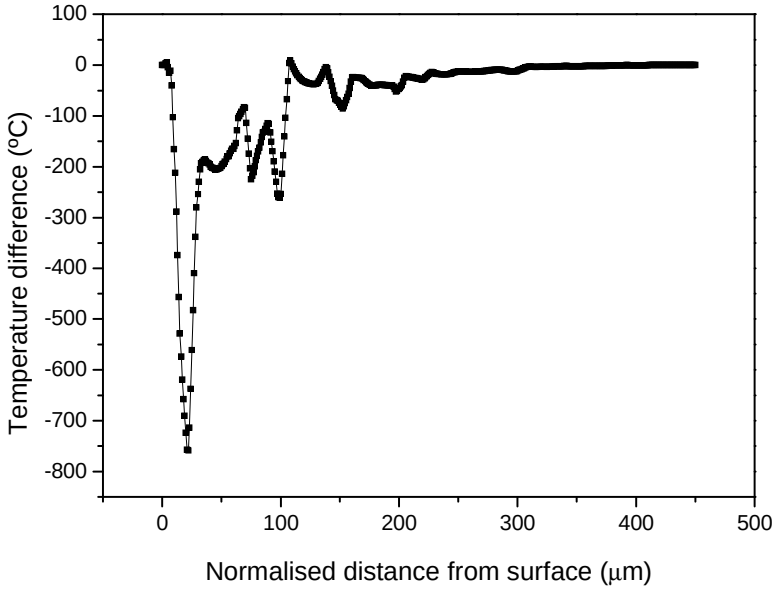

Fig. 5.42. Difference in temperature, along Z, between the profiles obtained for r=0.108 and 0.215 mm.

In Fig. 5.43 is plotted the temperature evolution with time, for the same element located at the surface in the central-most region of the plane shown in the images. The differences in the heating rates for different laser beam radius are evident. The element evaporated after 0.62, 149.6 and 291.1 ms for r=0.108, 0.162 and 0.215 mm, respectively. The estimated linear

heating rates were 6403, 2617 and 1321°C/ms for r=0.108, 0.162 and 0.215 mm, respectively.

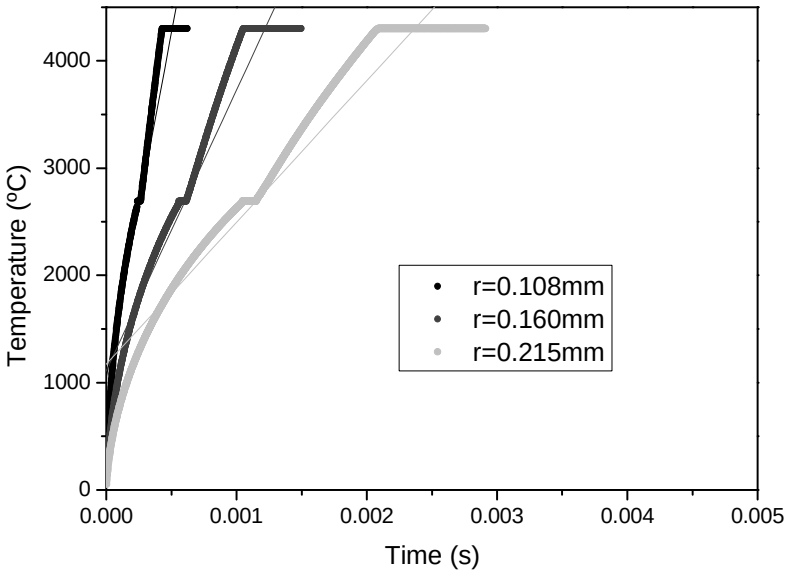

Fig. 5.43. Comparison of the temperature evolution with time of top-most element at the central-most section of the shown images. The straight lines represent the linear fitting for estimating the heating rates.

3.2. Mechanical analysis

The mechanical analysis has been done in models with 200x100 elements due to limitations of computing memory and a non-optimized code. Of course, the analyses were performed taking into account solely the elements in the solid phase. The following temperature and strain distribution profiles are neglecting the all elements with temperatures above the melting point (2690°C). The presented axial strain and stress results are only referring to horizontal direction (X). Moreover, three runs were carried out with models differing in porosity level in order to evaluate its influence on stress distribution.

3.2.1. Influence of porosity level

In Fig 5.45, Fig 5.46 and Fig 5.47 are shown the temperature and axial strain distribution profiles for workpieces with 0, 10 and 20% porosity, respectively. The positive and negative strain values, in the color bar scales, represent elongation and compression, respectively. It can be observed that regardless the porosity level, the highest tensile stresses are located in the center of the workpiece, where the thermal gradients are larger. Consequently, the compressive stresses will be mostly localized at the edges of the workpiece due to the imposed boundary conditions. The maximum tensile stress values are located in sharp peaks at the hottest regions at the surface. The maximum compressive stresses (negative values) are located in the valleys, mostly at the hottest regions. Comparing the three porosity levels, the increase in porosity results in higher heterogeneity in stress distribution.

The calculated maximum stress values are represented in Fig. 5.44. The increase in porosity resulted in an increase of the maximum axial stresses, both tensile and compressive. The maximum compressive stress values achieved were 4.9, 6.9 and 8.7 for 0, 10 and 20%, respectively, and the maximum tensile stresses were 10.1, 12.0 and 12.2 for 0, 10 and 20%, respectively.

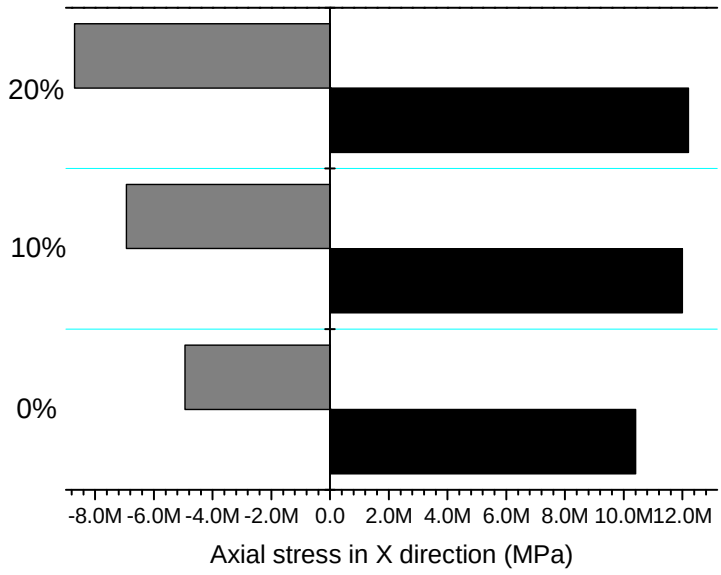

Fig. 5.44. Maximum axial stresses (compressive and tensile) reached for different levels of porosity.

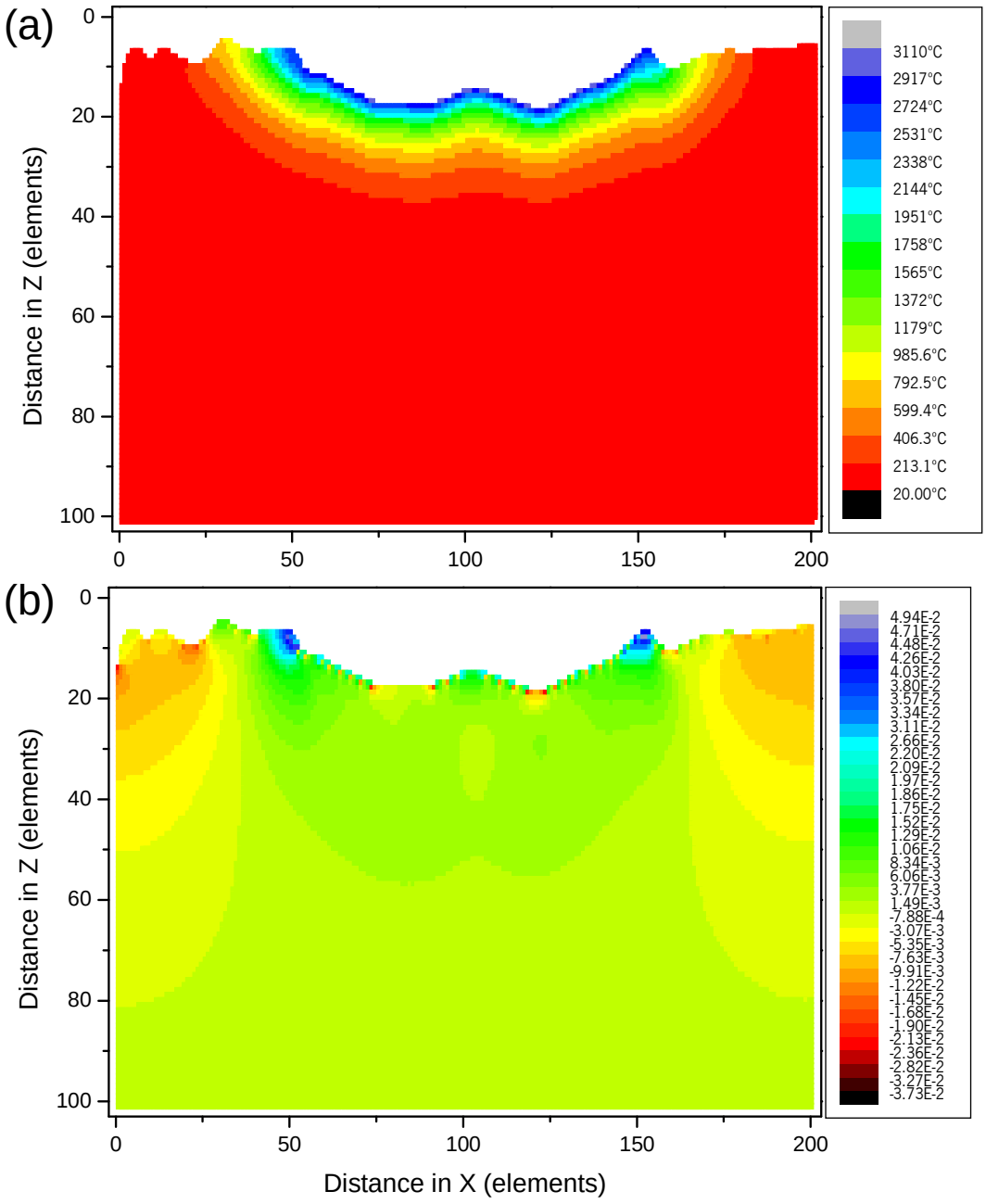

Fig 5.45. Temperature distribution (a) and respective axial strain distribution (parallel to X axis) (b), for a workpiece with 0% porosity.

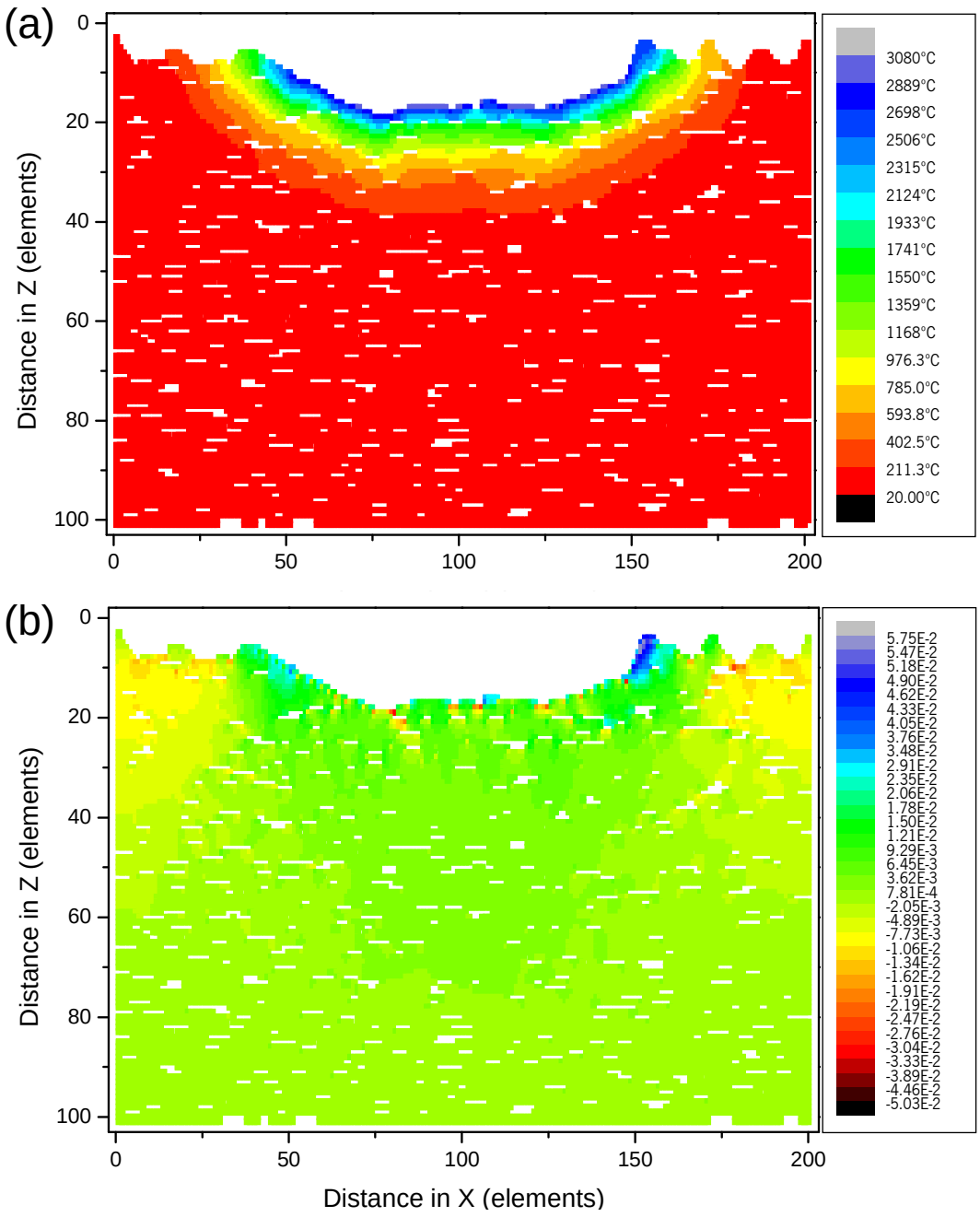

Fig 5.46. Temperature distribution (a) and respective axial strain distribution (parallel to X axis) (b), for a workpiece with 10% porosity.

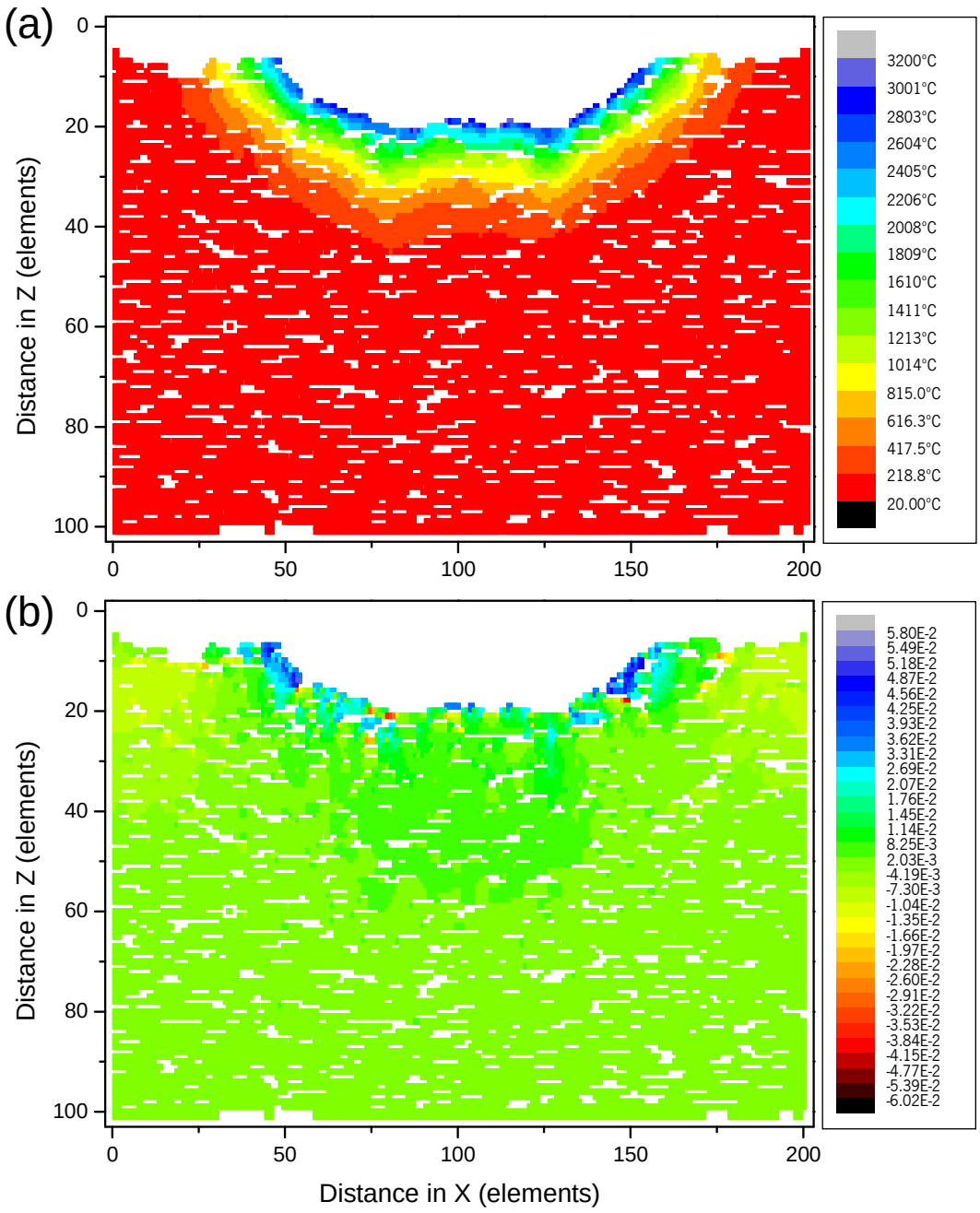

Fig 5.47. Temperature distribution (a) and respective axial strain distribution (parallel to X axis) (b), for a workpiece with 20% porosity.

4. Conclusions

A model designed for the simulation of the laser glazing of thermal barrier coatings was presented. It has been included mesoscopic details of typical plasma-sprayed TBCs, like the surface morphology and porosity. The model consisted on both thermal and mechanical analysis. Regarding the thermal analyses, it has been studied the influence of using temperature-dependent properties, the influence of the absorption coefficient, porosity level and laser beam spot size on the temperature and phase distribution within the workpiece, heating rates and size of the molten layer.

As observed for all the analyses, the temperature gradient evolves rapidly near the surface as the laser heating progresses. The energy gain due laser heating is considerably higher than the energy losses due to evaporation and conduction and therefore the temperature increase at the surface of the material is very rapid.

The use of temperature-dependent properties in this kind of analysis has a profound influence on the heating process and consequently on the final results. The absorption coefficient and aser beam radius have also a strong influence on the heating process since they affect considerably the energy density delivered by the beam and the energy density absorbed, respectively. The porosity has shown to have an important role on the heat conduction, however its influence should be more adequately evaluated by introducing fluid flow which would result in densification of the material.

Concerning the mechanical analyses, it was observed that regardless the porosity level, the highest tensile stresses are located in the center of the workpiece, where the thermal gradients are larger. The maximum tensile stress values are located in sharp peaks at the hottest regions at the surface. The maximum compressive stresses (negative values) are located in the valleys, mostly at the hottest regions. The increase in porosity resulted in an increase of the maximum axial stresses, both tensile and compressive.

5. Suggestions for the improvement of the model

In order to improve the results to achieve a more realistic simulation, below are listed some suggestions to be considered and implemented in the model.

- The porosity of the ceramic workpiece is assumed to be comprised of empty voids, i.e. does not consider the absorption of energy by the gases constrained inside the pores. Moreover, the contribution of the pressure generated inside the pores to the overall stress state is not considered.

- Heat transfer by convection at the moving interfaces solid/liquid and liquid/gas is not considered.

- Some of the energy of the laser could be absorbed or scattered by the gas plume formed at the surface which might obstruct or defocus the beam, particularly when dealing with CO_2 lasers [42].

- It is not considered variation of the absorption of the beam energy with temperature of the workpiece.

- It has not been included in this model the fluid flow of the molten material. It was planned to perform fluid flow to the empty voids (pores) due to gravity and capillarity and surface tension within the molten body [20, 31]. The dependence of the viscosity with temperature should also be considered.

References

[1] J.F. Li, L. Li and F.H. Stott, International Journal of Heat and Mass Transfer 47 (2004) 1159-1174.

[2] C. Batista, A. Portinha, R.M. Ribeiro, V. Teixeira, M.F. Costa and C.R. Oliveira, Applied Surface Science 247 (2005) 313-319.

[3] C. Batista, A. Portinha, R.M. Ribeiro, V. Teixeira, M.F. Costa and C.R. Oliveira, Surface and Coatings Technology 200 (2006) 2929-2937.

[4] C. Batista, A. Portinha, R.M. Ribeiro, V. Teixeira and C.R. Oliveira, Surface and Coatings Technology Volume 200 (2006) 6783-6791.

[5] I. Zaplatynsky, Thin Solid Films 95 (1982) 275-284.

[6] P.C. Tsai, H.L. Tsai and D.C. Tu, Materials Science and Engineering a-Structural Materials Properties Microstructure and Processing 165 (1993) 167-173.

[7] H.L. Tsai and P.C. Tsai, Surface and Coatings Technology 71 (1995) 53-59.

[8] S. Ahmaniemi, P. Vuoristo and T. Mantyla, Surface and Coatings Technology 151-152 (2002) 412-417.

[9] G. Antou, F. Hlawka, A. Cornet, C. Becker, D. Ruch and A. Riche, Surface & Coatings Technology 200 (2006) 6062-6072.

[10] S.O. Chwa and A. Ohmori, Surface and Coatings Technology 153 (2002) 304-312.

[11] S.O. Chwa and A. Ohmori, Surface and Coatings Technology 148 (2001) 87-94.

[12] K.C. Chang, W.J. Wei and C. Chen, Surface and Coatings Technology 102 (1998) 197-204.

[13] A. Koc, B.S. Yilbas, Y. Koc, S. Said, S.A. Gbadebo and M. Sami, Optics and Lasers in Engineering 30 (1998) 327-350.

[14] A. Koc, Heat and Mass Transfer 40 (2004) 697-706.

[15] T. Kato and H. Fujii, International Journal of Machine Tools and Manufacture 44 (2004) 927-931.

[16] K. Dai and L. Shaw, Acta Materialia 52 (2004) 69-80.

[17] L. Hao and J. Lawrence, Journal of Materials Processing Technology 180 (2006) 110-116.

[18] H.-T. Hsu and J. Lin, International Journal of Machine Tools and Manufacture 45 (2005) 979-985.

[19] Y. Hu, Z. Yao and J. Hu, Surface and Coatings Technology 201 (2006) 1426-1435.

[20] M. Leung, Journal of Physics D-Applied Physics 34 (2001) 3434-3441.

[21] J.F. Li, L. Li and F.H. Stott, International Journal of Heat and Mass Transfer 47 (2004) 5523-5539.

[22] J.F. Li, L. Li and E.H. Stott, Journal of the European Ceramic Society 24 (2004) 3509-3520.

[23] J.F. Li, L. Li and F.H. Stott, Journal of Physics D-Applied Physics 37 (2004) 1710-1717.

[24] J.F. Li, L. Li and F.H. Stott, Journal of the European Ceramic Society 24 (2004) 3509-3520.

[25] A.P. Mackwood and R.C. Crafer, Optics & Laser Technology 37 (2005) 99-115.

[26] L. Pawlowski and I. Smurov, Surface and Coatings Technology 151-152 (2002) 308-315.

[27] A.A. Peligrad, E. Zhou, D. Morton and L. Li, Optics & Laser Technology 33 (2001) 7-13.

[28] D. Triantafyllidis, L. Li and H. Stott, Journal of the American Ceramic Society 89 (2006) 1286-1294.

[29] A. Vila Verde, M.M.D. Ramos, R. Mendes Ribeiro and M. Stoneham, Thin Solid Films 453-454 (2004) 89-93.

[30] A. Vila Verde, M.M.D. Ramos, M. Stoneham and R. Mendes Ribeiro, Applied Surface Science 238 (2004) 410-414.

[31] L.X. Yang, X.F. Peng and B.X. Wang, International Journal of Heat and Mass Transfer 44 (2001) 4465-4473.

[32] A.A. Peligrad, E. Zhou, D. Morton and L. Li, Surface and Coatings Technology 150 (2002) 15-23.

[33] A. Powell. Course Materials, MIT, Massachussetts Institut of Technology, http://mightylib.mit.edu, 2002.

[34] S.S. Rao, The Finite Element Method in Engineering, Butterworth-Heinemann 2005.

[35] H. Saunders, Journal of Pressure Vessel Technology-Transactions of the Asme 106 (1984) 421-422.

[36] H. Oertel, American Scientist 72 (1984) 526-526.

[37] H. Saunders, Journal of Pressure Vessel Technology-Transactions of the Asme 106 (1984) 127-127.

[38] A. Portinha, V. Teixeira, J. Martins, M.F. Costa, R. Vassen and D. Stoever. in Advanced Research Workshop on Nanomaterials and Coatings, NATO series E-Appl. Science, Kluwer Academic Publishers, Kiev 2002.

[39] http://www.matweb.com.

[40] G. Lins and D.W. Branston, Surface and Coatings Technology 116-119 (1999) 1249-1253.

[41] Non-contact temperature measurement, Transactions in Measurement and Control, Vol. Volume 1, 2nd Edition, Putman Publishing Company and OMEGA Press LLC 1998.

[42] B.-L. Wang and Y.-W. Mai, International Journal of Mechanical Sciences 47 (2005) 303-317.

[43] J. Lawrence and L. Li, Applied Surface Science 168 (2000) 71-74.

[44] J. Lawrence, K. Minami, L. Li, R.E. Edwards and A.W. Gale, Applied Surface Science 186 (2002) 162-165.

[45] R.J. LeVeque, Finite Difference Methods for Differential Equations, University of Washinghton, AMath 585-586, Lecture Notes 2005.

[46] A.K. Kaw, An interactive e-book for illustrating Finite Difference Method of solving ordinary differential equations, Holistic Numerical Methods Institute, College of Engineering, University of South Florida 2006.

[47] http://en.wikipedia.org/wiki/Heat_conduction.

[48] J. Lawrence and L. Li, Surface and Coatings Technology 162 (2003) 93-100.

[49] T. Pang, An Introduction to computational physics, 1st ed., Cambridge University Press 1997.

[50] N.P. Padture, M. Gell and E.H. Jordan, Science 296 (2002) 280-284.

[51] A. Portinha, V. Teixeira, J. Carneiro, J. Martins, M.F. Costa, R. Vassen and D. Stoever, Surface and Coatings Technology 195 (2005) 245-251.

[52] B. Roge, A. Fahr, J.S.R. Giguere and K.I. McRae, Journal of Thermal Spray Technology 12 (2003) 530-535.

[53] D.D. Hass, Directed Vapor Deposition of Thermal Barrier Coatings, PhD Thesis, University of Virginia (2000).